Article

Processes Associated with Multiphase Dolomitization and Other Related Diagenetic Events in the Jurassic Samana Suk Formation, Himalayan Foreland Basin, NW Pakistan

Hamad-ur- Rahim [1,2], Shazia Qamar [1,3], Mumtaz Muhammad Shah [1,*], Mercè Corbella [4], Juan Diego Martín-Martín [5], Hammad Tariq Janjuhah [6,*], Dídac Navarro-Ciurana [4,5], Vasiliki Lianou [7] and George Kontakiotis [7]

1   Department of Earth Sciences, Quaid-i-Azam University, Islamabad 45320, Pakistan
2   Earth Sciences Division, Pakistan Museum of Natural History, Islamabad 44000, Pakistan
3   Institute of Geology, University of Azad Jammu and Kashmir, Muzaffarabad 13100, Pakistan
4   Departament de Geologia, Facultat de Ciencies, Universitat Autonoma de Barcelona, Edifici Cs s/n, 08193 Bellaterra, Spain
5   Departament de Mineralogia, Petrologia i Geologia Aplicada, Facultat de Geologia, Universitat de Barcelona (UB), Martí i Franquès s/n, 08028 Barcelona, Spain
6   Department of Geology, Shaheed Benazir Bhutto University, Sheringal 18050, KP, Pakistan
7   Department of Historical Geology-Paleontology, Faculty of Geology and Geoenvironment, School of Earth Sciences, National and Kapodistrian University of Athens, Panepistimiopolis, Zografou, 15784 Athens, Greece
*   Correspondence: mshah@qau.edu.pk (M.M.S.); hammad@sbbu.edu.pk (H.T.J.)

Abstract: Foreland fold and thrust belts always represent a complex diagenetic history of carbonate succession, particularly multiphase dolomitization, due to the multi-sourcing nature of fluids affecting syn-to post-depositional successions. The present work documents a comprehensive study on the diagenetic changes, particularly dolomitization patterns in the Jurassic carbonates (Samana Suk Fm) in the Lesser Himalayan fold and thrust belt, NW Pakistan. To better understand the processes involved, integrated field/petrographic, geochemical, isotopic, and micro-thermometric studies were carried out. Field observations indicate that dolostones appear as light grey to brown stratabound and patchy units within the formation. Petrographic analysis reveals that fabric destructive matrix dolomite (RD-I) and fabric preserving replacive dolomite (RD-II) phases are present as distinct units. In addition, saddle dolomite cement (SD) and fracture-filling calcite (CC) are also observed in association with replacive dolomite cement. Geochemical analysis (EPMA) showed that Fe, Mn, and Ba concentrations in matrix dolomite are relatively less than those of replacive/saddle dolomite and fracture-filling calcite, suggesting a hydrothermal source of replacive/saddle dolomite in reducing conditions. Furthermore, stable isotope studies of RD-I showed non-depleted $\delta^{18}O$ values, which represent coeval seawater signatures of Jurassic carbonates. RD shows depleted $\delta^{18}O$ values and non-depleted $\delta^{13}C$, respectively, indicating burial or elevated temperature of dolomitization. Fracture-filled calcite represents lighter $\delta^{18}O$ values and $\delta^{13}C$, indicative of relatively high temperatures. $^{87}Sr/^{86}Sr$ ratios of all diagenetic phases range from 0.707718 to 0.710747, showing more radiogenic values indicates interaction fluids with more radiogenic sources. Fluid inclusion micro-thermometry data of saddle dolomite shows T_H ranging from 102.8 to 186 °C, and salinity ranging from 11.7 to 19.4 eq. wt.% NaCl, suggesting hot saline brines are responsible for the dolomitization. Fracture-filling calcite shows T_H ranging from 68.0 to 98.4 °C and salinity ranging from 6.9 to 13.1 eq. wt.%. NaCl suggests moderately hot and saline solutions are responsible for their formation. In conclusion, the above-mentioned studies indicate two distinct processes of dolomitization are involved in the formation of matrix and replacive/saddle-type dolomites. RD-I has formed in the evaporative setting, whereas RD has formed due to the interaction of hydrothermal fluids during burial. Fracture-filling calcite is produced from hot subsurface solutions during uplift related to the Himalayan orogeny.

1. Introduction

Dolomitization of platform carbonate successions commonly results from multi-phase replacive processes of limestones [1–4]. The topic has been the object of intensive research during the last decades due to its close association with major hydrocarbon reservoirs and other economic mineral resources such as MVT and SEDEX mineralization [2,5–8]. Extensive exploration examples of the Paleozoic dolomite reservoirs are well known [9–11], but there are only a few case studies where Mesozoic dolomites are extensively studied [4,12–14]. The key factors controlling the occurrence and distribution of these Mesozoic dolomites are as yet poorly understood, and their outcrop analogs are less extensively studied.

Most of the known massive dolomites have important tectonic control, usually formed in extensional settings [2,3,5–9]. These are commonly called structurally controlled dolomites, which usually involve hot fluids formed when the fluids have a temperature higher than the host rock [2,6]. These structural dolomites usually form a variety of geometries similar to a Christmas tree [6]. However, later recrystallization and hydrothermal alteration usually obscure the original dolomite signatures.

In North Pakistan, the Jurassic shelf carbonates of Samana Suk Fm are composed of oolitic, pellitic, and fossiliferous limestone deposited in high energy conditions [4,15]. There is massive dolomitization observed in the Jurassic carbonates of Samana Suk Fm, but this study was limited to the single outcrop unit [4,15]. This paper presents the first comprehensive study to interpret the dolomitization mechanism in the Jurassic carbonates of Samana Suk Fm by using a multi-proxy approach. In Pakistan, the middle Jurassic Samana Suk Fm is proven as a good reservoir rock in the Hazara basin and adjacent Indus Basin, as documented by various researchers [15–20]. Therefore, this paper can serve as a model for the exploration of diagenetically altered Jurassic carbonate reservoirs in the area and around the world.

2. Geological Setting

The area under investigation is part of the extensive Lesser Himalayan fold and thrust belt known as the Attock Hazara Fold and Thrust Belt (AHFTB) that developed because of the Cenozoic collision between Indian and Eurasian plates [21–26]. Three hill ranges, namely Hazara, Margalla, and Kala Chitta, are selected in the present study (Figure 1).
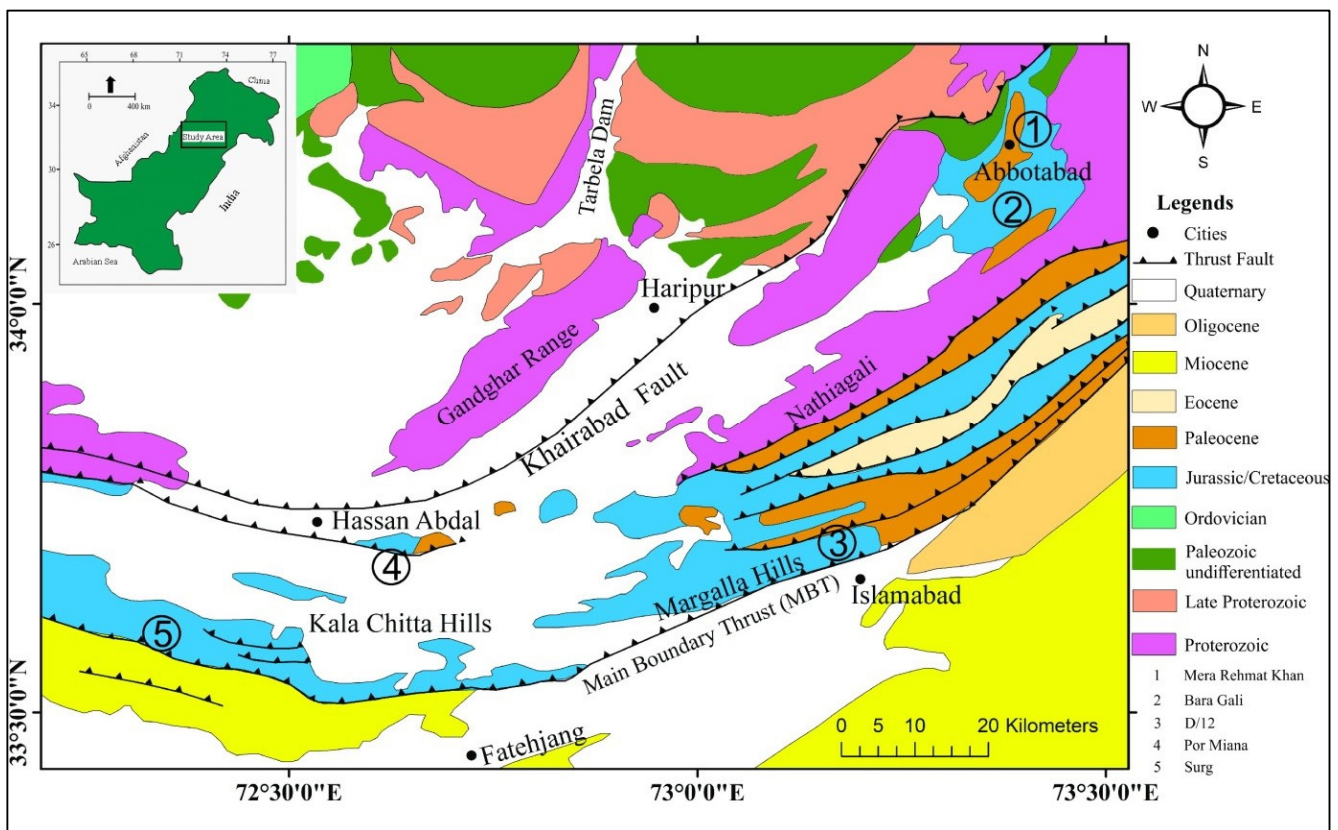
Figure 1. Geological map of the study area showing the location of studied sections modified from Searle et al. [27].

The sedimentary succession cropping out in the area ranges from Precambrian to Pleistocene, punctured by pronounced hiatuses as reported by various workers [23,28,29] (Figure 2). The Jurassic succession appears above the Pre-Cambrian rocks. The Jurassic succession consists of the Baroch Group, comprising Datta FM and Samana Suk FM. The carbonate Samana Suk Fm has a lower transitional contact with the sandstones of Datta Fm and is uncomfortably overlain by the Cretaceous Chichali Fm [23,29–31] (Figure 2).

The Samana Suk Formation was deposited on the stable platform on the NW part of the Indian plate during greenhouse conditions [23,32]. After the deposition of Middle Jurassic Samana Suk Fm, the Indian plate detached from the Gondwanaland, and an extensional regime prevailed in the study area up to the late Cretaceous [33,34]. During this time, restricted depositional environments prevailed over the Indian plate. During Early Cretaceous times, the Indian plate passed over the Ninety-East Keregulen hotspot and experienced domal uplift, which caused detritus to spread widely in the basins of the Indian plate. The Lumshiwal sandstone of the Late Cretaceous age was deposited during this time. Later on, this activity resulted in the eruption of Rajmahal Traps [35,36].

The Cretaceous–Paleogene time is considered a very important period in the paleogeographic history of the Indian plate. Firstly, the ophiolite emplacement took place during the Cretaceous time [37]. Secondly, the collision of the Kohistan Island Arc (KIA) and the Indian plate occurred. Thirdly, the final closure of Neo-Tethys along the Indus-Tsangpo suture occurred in the Paleocene–Eocene time, too, resulting in the final collision and formation of the world's largest mountain system, called the Himalayas [38].
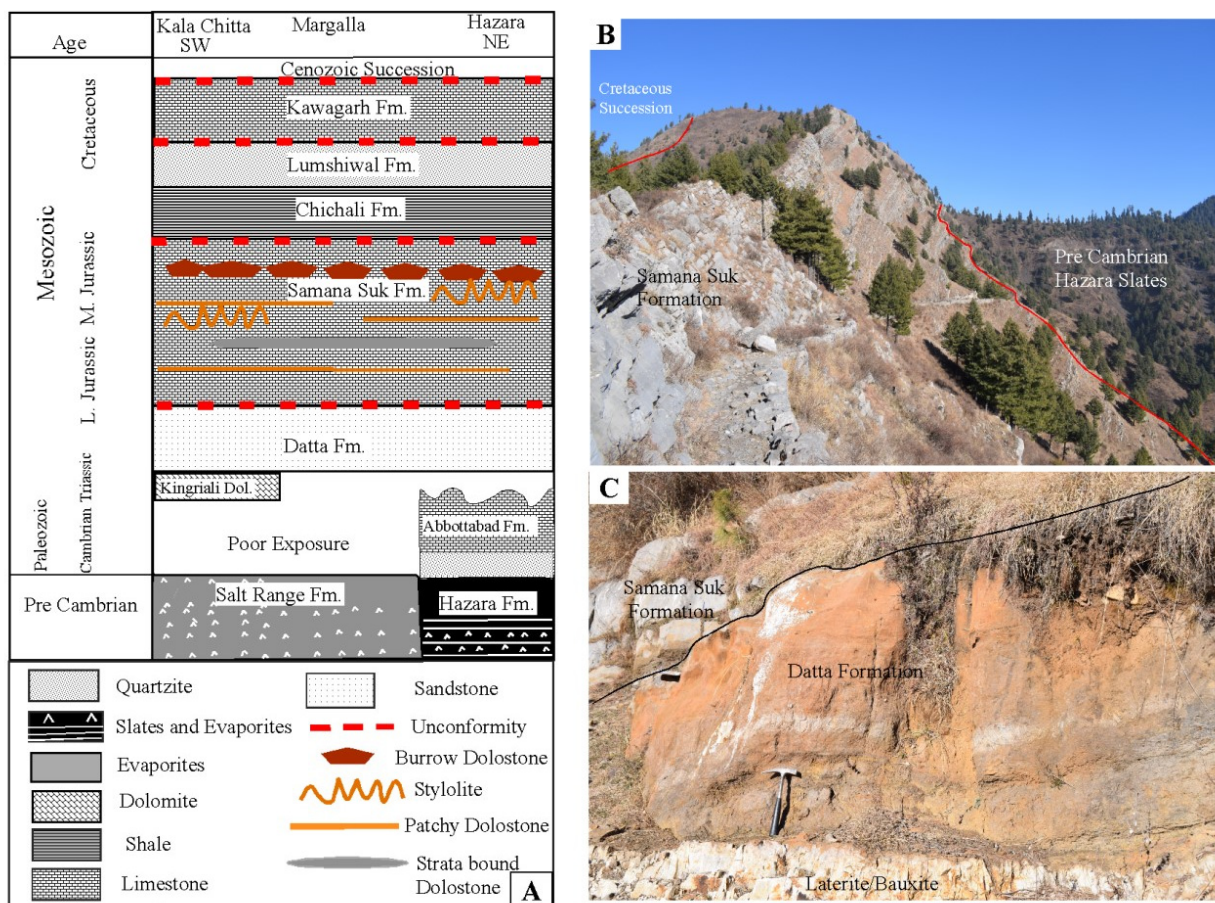
Figure 2. (**A**) The lithostratigraphic column of the Lesser Himalayas represents the major Mesozoic stratigraphic units and pronounced hiatuses (modified after Ahsan et al., [28]). Note that dolomitization only affects the Samana Suk Formation. (**B**) A panoramic photograph of the Samana Suk Formation representing top and bottom contacts. (**C**) Bottom contact of the Samana Suk Formation with the Datta Formation. Laterite/bauxite horizons are observed in the Datta Formation.

The Jurassic sequence consists of the Datta Formation and Samana Suk Formation, which is the oldest exposed succession of the Cenozoic era in all parts of the Lesser Himalayas (Hazara Hills, Kala Chitta Hills, and Margalla Hills) [15,18,28,29] (Figure 2).

Within the carbonate succession of the hill ranges of the Lesser Himalayas, dolomitization is reported in the Middle Jurassic Samana Suk Fm and upper part of the Datta Formation but is not reported in the Cretaceous or Paleogene rock units [32] (Figure 2). The Samana Suk Fm is composed of thin-to-thick bedded limestone with small intercalations of marl [39]. The limestone is mostly oolitic, fossiliferous, and micritic, deposited in lagoonal, intertidal, and shoal environments [32,40,41].

3. Methodology

The lithological units were selected in areas where the Middle Jurassic Samana Suk Formation is well exposed. Extensive field exploration and detailed sampling were carried out from five outcrops located in the Lesser Himalayas to study the dolomitization of the Jurassic Samana Suk Formation (Figure 2). These outcrops are (1) Mera Rehmat Khan (34°14′33″, 73°20′29″), (2) Baragali (34°06′02″, 73°20′41″), (3) Shah Allah Ditta, Islamabad (33°43′30″, 72°56′49″), (4) Pormiana (33°54′53″, 72°43′09″), and (5) Surg (33°42′11″, 72°43′09″).

More than 200 thin sections were prepared and examined using an Olympus CX31 microscope mounted with a DP-21 camera attachment at the Department of Earth Sciences, Quaid-i-Azam University, Islamabad, Pakistan. The studied dolomite and calcite crystal

textures were described using the Sibley and Gregg [42] classification schemes as modified by Flügel-Martinsen [43]. A cathodoluminescence microscopic study (CL) was performed on 36 selected thin sections using CITL (MK5-1) model cold-cathode optical CL equipment with an attached Nikon Eclipse 50iPOL microscope mounted with a Nikon DS-Ri1 camera at the Department of Mineralogy, Petrology and Applied Geology, University of Barcelona, Spain.

Polished thin sections were prepared and coated with carbon for the analysis of major and trace elements (Ca, Mg, Fe, Mn, Na, Sr, Zn, Ba) under an electron microprobe equipped with a wavelength dispersive spectrometer (WDS) at the University of Barcelona. The detection limits of different elements are as follows (Ca = 269 ppm), (Mg = 347), (Fe = 116 ppm), (Mn = 122 ppm), (Na = 128 ppm), (Sr = 467 ppm), (Zn = 157 ppm), (Ba = 176 ppm) (Table 1).

Stable carbon and oxygen isotope analyses were carried out on 57 different dolomite and calcite samples representing different diagenetic phases. They are separated with the help of a micro drill bit size of 0.5–1 mm. Isotopic analysis was carried out at the Center of Science and Technology (CCiT), University of Barcelona (UB). About 50–60 mg of powder were reacted with 100% phosphoric acid (density >1.9; Wachter and Hayes (1985) at 75 °C in an online carbonate preparation line (Carbo-Kiel—single-sample acid bath) connected to a Finnigan MAT 252 mass spectrometer. Rosenbaum and Sheppard [44] gave fractionation factors that were used to correct the isotopic composition values of dolomite.

The Sr isotopic ratio ($^{87}Sr/^{86}Sr$) of 8 powdered dolomite and calcite samples were analyzed at the Geochronology and Isotope Geochemistry Service, University Complutense de Madrid, Spain (Table 2). Samples were prepared using the following procedure. A total of 50 mg of each sample was dissolved in 7 mL of 2.5 N HCl and placed in an oven at 120 °C for 65 h. Once samples were completely dried, 1 mL of ultra-pure HNO_3 was added and set back on the heat plate. Then, 3 mL of HNO_3 3 M was added to the samples, which were ready for chromatographic separation. Chromatographic separation of Sr from Rb and sample matrix was performed using an extraction resin. Sr samples were recovered in 1 μL of 1 M phosphoric acid and loaded, together with 2 μL of Ta_2O_5, onto a degassed single filament of Re. Sr analyses were performed on an Isotope X-Phoenix (TIMS) following a dynamic multi-collection method for 160 cycles, with a stable ion intensity of 3 V in the mass ^{88}Sr. Possible ^{87}Rb interferences were corrected in the Sr analysis, and the $^{87}Sr/^{86}Sr$ ratio was normalized in order to correct for mass fractionation, taking into account a reference value of $^{86}Sr/^{88}Sr$ = 0.1194. The NBS 987 Sr isotopic standard was checked along with the samples, yielding the results.

Fluid inclusion micro-thermometric studies were carried out on five doubly polished wafers prepared by using the method of Roedder [45]. Micro-thermometric measurements were carried out using a Linkam THMS-600 heating and cooling stage installed at the Department of Geology of the Autonomous University of Barcelona (UAB). The calibration of the stage was performed using a synthetic material of a known composition. Due to the vulnerable nature of carbonate rocks, homogenization temperature (T_H) was measured before the last ice melt (T_{mi}). Since it is considered that the homogenization temperature (T_H) is close to the minimum trapping temperature (T_t), no pressure correction was applied. The measured T_{mi} is used to calculate the salinity in wt.% equivalent to NaCl using the Bodnar et al. [46] equation.

4. Results

4.1. Field Investigations and Petrographic Studies

The middle Jurassic Samana Suk Formation is composed of oolitic limestone with small patches of shale. The limestone is mostly deposited in high energy conditions in platform settings with periodic fluctuations [47–49]. Dolomitization is the most common diagenetic process in the Samana Suk Formation. Dolostones are easily identified in the field based on color contrast with the host limestone (Figure 3). Two types of dolomitization patterns are observed in the field: (i) light grey to light brown completely dolomitized horizons; (ii) rusty brown patchy dolomitized horizons clearly observable due to distinct

color contrast (Figure 3C). The dolomite fronts are roughly parallel to the stratification and cross-cutting in a few places (Figure 3C,D). The contact between the host limestone and dolostone is usually sharp and abrupt (Figure 3C). Dolostones are roughly concordant to the bedding planes and sometimes cross-cut the bedding at a steep angle (Figure 3C,D). Patchy dolomite bodies mostly follow weak planes such as the bedding, stylolites, burrows, and fracture planes present in the stratification (Figure 3E,H). Dolomites usually contain the relicts of host limestone (Figure 3G). Dolomites are further cross-cut by, and thus postdated by, fracture-filling calcite (Figure 3G). The observed dolomites of the studied formation were affected by the weathering process of surficial fluids, which resulted in their dedolomitization. These dedolomites usually appear rusty brown in the outcrop (Figure 3G).
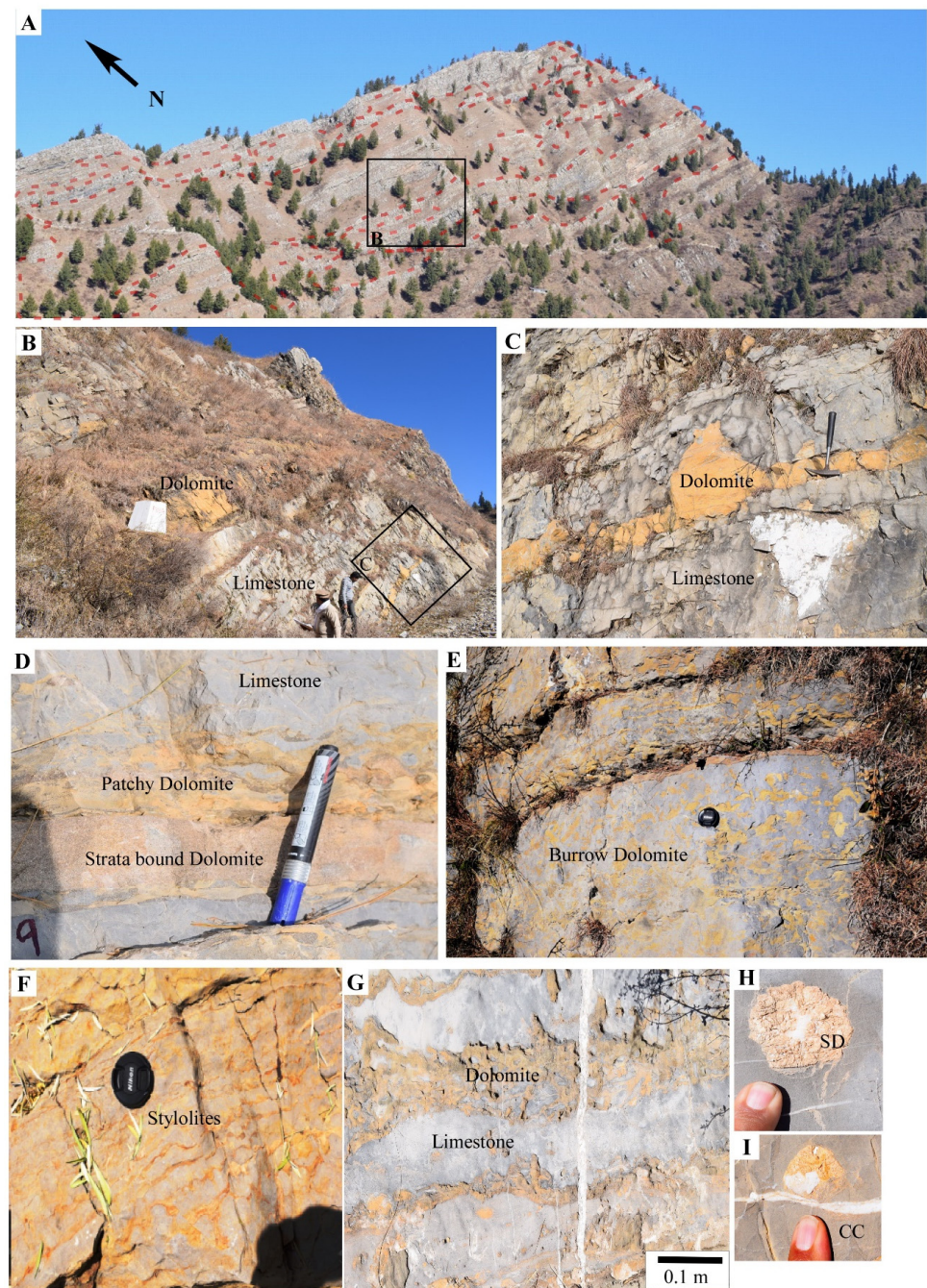

Figure 3. Outcrop photographs of the Samana Suk Formation show the different patterns of dolomitization.

(**A**) A panoramic photograph of the outcrop of the Samana Suk Formation at Mera Rehmat Khan section, Hazara area. The dashed red line represents the dolomitization observed in the formation. (**B**) An inset image shows the dolomitization patterns observed. (**C**) Inset image of patchy brown dolomites after stratification. (**D**) Detailed view of strata-bound dolostone and patchy dolostone in contact with the host limestone. (**E**) Burrows are filled with brown dolomite as a result of the replacement process, differential weathering making them prominent and showing positive relief features. (**F**) Bedding consists of parallel stylolites filled with patchy brown dolomite. Note that the brown dolomites are present in the open stylolites. (**G**) Light grey limestone and patchy brown dolomites are cross-cut by the fracture-filling calcite. (**H**) Pore-filling saddle dolomite exhibiting large crystal size. (**I**) Cream-colored pore-filling saddle dolomite and fracture-filling calcite in the matrix dolomite.

In the microscopic studies, different types of dolomites are identified based on the classification scheme of Sibley and Gregg [42] based on crystal shape, texture, and morphology. Two types of dolomite are distinguished: (i) matrix replacive dolomites (RD-I) and (ii) replacive dolomites (RD-II) (Figure 4). Matrix replacive dolomite (RD-I) is a fine crystalline anhedral to euhedral variety with closely packed crystals of size 20 to 40 μm. This variety completely obscures the host limestone features (Figure 4A,B). Replacive dolomite (RD-II) occurs as a void-filling replacive phase with a large euhedral crystal size ranging from 40 to 80 μm. The crystals are zoned with cloudy cores and clear rims (Figure 4C,D). The saddle dolomite (SD) occurs as a cementing phase within the void spaces (Figures 3H,I and 4E,F). This variety is of the largest crystal size, ranging from 1000 to 5000 μm. The variety shows undulose extinction when observed under cross-polarizing light. The variety also has ghosts of different varieties of dolomite crystals showing an evident cross-cutting relationship. The identified calcite is mainly fracture-filling calcite (CC), cross-cutting both host limestone and dolomite at very steep angles. The limestone is blocky in nature, with large crystal sizes ranging from 500 to 1000 μm.

4.2. Geochemistry

4.2.1. Major and Trace Elements

EMP (Electron Microprobe) analyses were carried out on different diagenetic phases observed in the Samana Suk Formation (Table 1). The Samana Suk Formation host limestones show a CaO content ranging from 45.99 to 59.57 Wt.% (*n* = 19, average 54.48 Wt.%). The Mg concentration ranges from 0.341 to 0.940 wt.% MgO; *n* = 19, with an average concentration of 0.60 Wt.% MgO. Na concentrations range from bdl to 886 ppm, with an average of 316 ppm for *n* = 19. Fe concentrations range from 1002 to 2576 ppm (*n* = 19), with a mean of 1490 ppm. Mn concentrations range from bdl to 608 ppm; the average for *n* = 19 is 175 ppm. The Zn concentration ranges from bdl to 287 ppm; *n* = 19, average bdl. The Ba concentration is below the detection limit (Figure 5A,B).

The matrix dolomite (RD-I) has a CaO concentration ranging from 30.8 to 38.28 Wt.% (*n* = 36; average 33.24 Wt.%). The MgO concentration ranges from 11.43 to 18.55 wt.% (*n* = 36; average 17.15 Wt.%). The average Na concentration ranges from bdl to 1396 ppm (average 533 ppm). The concentration of Fe ranges from 4159 to 17,101 ppm (with an average of 9518 ppm).

Mn concentrations range from bdl to 651 ppm, with 227 ppm being the average. The average Zn concentration ranges from bdl to 183 ppm. The concentration of Ba ranges from bdl to 751 ppm, with an average of 196 (Figure 5A,B).
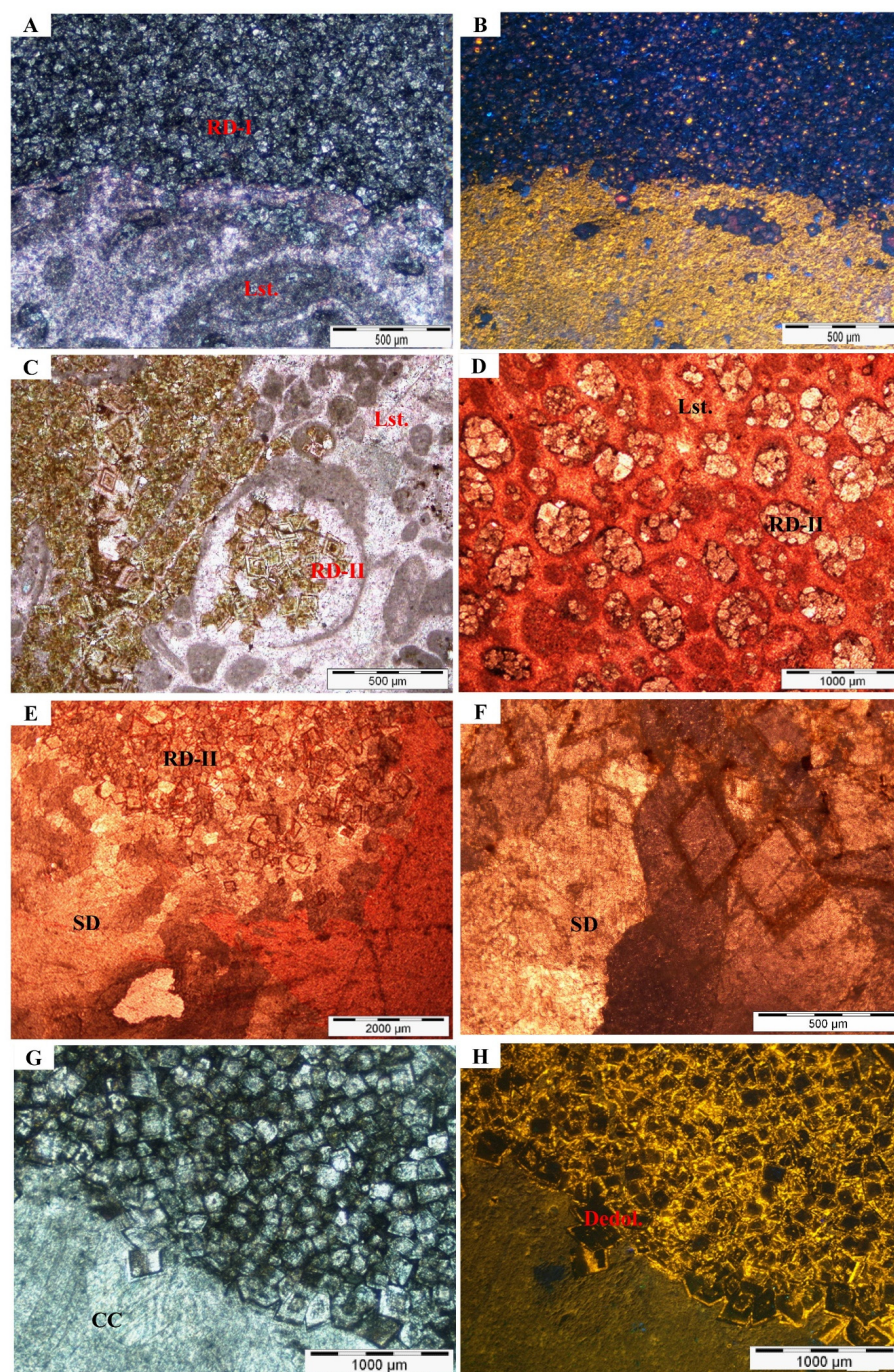
Figure 4. Petrographic features of the dolomite phases observed in the formation. (**A,B**) XPL and corresponding CL photomicrographs of the matrix dolomite (RD-I) show its small crystal size and non-luminescent nature. Note that the bright yellow nucleus of the dolomite crystal growth is clearly visible. (**C**) A PPL photomicrograph of the replacive dolomite cement (RD-II) following the weak planes; the plane nature and concentric growth along the crystals are clearly visible. (**D**) An XPL photomicrograph of a stained thin section shows the replacement dolomite cement (RD-II). Note that it is filling void spaces present in the host limestone. (**E**) An XPL photomicrograph of the saddle dolomite SD shows curved crystal faces and undoluse extinction present in association with the replacive dolomite (RD-II). (**F**). Inset detail photomicrograph of the saddle dolomite showing the crystal overgrowing the replacive dolomite RD-II. (**G,H**) The XPL and corresponding CL photomicrograph show the bright yellow luminescence of the crystal faces characteristic of dedolomtiztion. Note that the outer rims show brighter luminescence.

Table 1. EPMA data of limestone and dolomite phases of the Samana Suk Formation.

Sr. No	Sample No	Phase	Point No	CaO Wt.%	MgO Wt.%	Na (ppm)	Fe (ppm)	Mn (ppm)	Zn (ppm)	Ba (ppm)
1	DS-17	Host Limestone	27	50.03	0.6055	bdl	2576	216	bdl	bdl
2	DS-17	Host Limestone	32	45.99	8.64	258	11,815	0	bdl	682
3	DS-17	Host Limestone	38	55.24	0.8165	bdl	1244	123	bdl	bdl
4	DS-17	Host Limestone	39	54.82	0.4879	243	1283	153	bdl	bdl
5	DS-17	Host Limestone	40	53.27	0.9339	647	6668	24	225	bdl
6	DS-17	Host Limestone	57	55.39	0.3413	258	1002	231	bdl	bdl
7	DS-17	Host Limestone	45	53.99	1.2727	bdl	2040	248	bdl	bdl
8	DS-17	Host Limestone	46	55.32	0.16	bdl	721	84	bdl	bdl
9	DS-17	Host Limestone	66	55.01	0.4679	127	1673	222	bdl	bdl
10	DS-17	Host Limestone	73	54.63	0.8177	bdl	1684	89	0	bdl
11	DS-17	Host Limestone	74	54.97	0.5624	142	1606	139	bdl	bdl
12	MR-12	Host Limestone	106	54.32	0.5577	506	1228	bdl	0	bdl
13	MR-12	Host Limestone	107	53.87	0.7406	bdl	1152	197	0	bdl
14	MR-12	Host Limestone	108	53.89	0.4652	573	2291	137	8	bdl
15	MR-12	Host Limestone	109	53.37	0.5793	550	1714	192	172	bdl
16	MR-8	Host Limestone	141	52.67	0.9402	175	1723	608	0	bdl
17	MR-8	Host Limestone	142	55.23	0.4701	320	1109	bdl	230	bdl
18	MR-8	Host Limestone	143	54.19	0.4582	886	1020	202	0	bdl
19	MR-8	Host Limestone	144	59.57	0.5598	525	1058	bdl	287	bdl
20	DS-17	RD-I	26	32.78	17.14	634	10,105	261	bdl	bdl
21	DS-17	RD-I	28	32.94	16.96	477	15,468	651	bdl	bdl
22	DS-17	RD-I	29	33.85	16.44	655	15,391	368	bdl	bdl
23	DS-17	RD-I	30	32.97	17.77	470	8375	83	bdl	bdl
24	DS-17	RD-I	31	32.35	18.55	138	6985	264	bdl	bdl
25	DS-17	RD-I	34	33	17.03	135	11,193	182	bdl	bdl.
26	DS-17	RD-I	35	33.4	17.69	bdl	7733	303	bdl	bdl.
27	DS-17	RD-I	36	32.68	18.33	438	5010	243	183	bdl
28	DS-17	RD-I	37	32.45	17.09	524	6368	98	0	bdl
29	DS-17	RD-I	41	32.49	17.81	390	17,101	298	bdl	bdl
30	DS-17	RD-I	42	32.26	17.32	473	11,660	343	bdl	bdl
31	DS-17	RD-I	43	32.87	17.76	729	7484	426	bdl	bdl
32	DS-17	RD-I	44	32.35	18.36	680	10,882	346	bdl	bdl
33	DS-17	RD-I	47	33.14	17.82	961	108,04	218	bdl	189
34	DS-17	RD-I	52	32.47	16.8	1003	13,836	229	167	498
35	DS-17	RD-I	53	32.89	17.59	398	8874	315	0	337
36	DS-17	RD-I	54	33.11	18.09	520	6839	147	bdl	0
37	DS-17	RD-I	55	33.33	17.51	1194	5832	54	118	0
38	DS-17	RD-I	61	33.03	17.74	421	11,426	341	2	0
39	DS-17	RD-I	62	30.8	17.91	1396	10,882	240	0	271
40	DS-17	RD-I	63	30.82	18.01	345	12,437	232	134	156
41	DS-17	RD-I	64	33.43	17.08	607	7376	348	132	0
42	DS-17	RD-I	70	32.44	17.45	755	15,002	354	0	0
43	DS-17	RD-I	71	31	18.38	357	12,048	364	180	119
44	DS-17	RD-I	72	33.54	17.86	361	7886	387	0	751
45	DS-17	RD-I	88	33.79	17.04	324	4159	54	0	0
46	MR-12	RD-I	90	34.63	16.31	859	7681	157	0	343
47	MR-12	RD-I	91	32.97	17.29	887	7461	0	0	528
48	MR-12	RD-I	96	34.81	16.27	422	9176	108	0	0
49	MR-12	RD-I	97	36.95	13.76	570	4529	21	0	0
50	MR-12	RD-I	98	38.28	11.43	385	8708	365	0	0
51	MR-12	RD-I	99	34.26	16.84	148	5803	28	25	606
52	MR-12	RD-I	100	34.69	15.87	361	12,670	35	49	321
53	MR-12	RD-I	101	33.63	17.24	198	8002	76	0	228
54	MR-12	RD-I	110	33.7	16.68	566	9732	75	bdl	0
55	MR-12	RD-I	111	32.67	18.19	318	7756	169	0	0
56	MR-8	RD-II	112	33.53	16.75	653	10,416	39	0	0
57	MR-8	RD-II	113	32.97	16.69	65	16,556	209	55	260
58	MR-8	RD-II	114	32.56	17.61	275	10,804	113	bdl	554
59	MR-8	RD-II	115	32.41	16.04	35	22,075	255	255	0
60	MR-8	RD-II	116	31.93	13.91	66	52,312	505	bdl	0
61	MR-8	RD-II	117	33.69	16.85	341	10,338	158	0	0
62	MR-8	RD-II	118	33.21	16.94	0	12,359	161	0	0
63	MR-8	RD-II	119	32.99	17.45	472	9444	bdl.	27	0
64	MR-8	RD-II	120	32.47	14.39	114	41,819	480	0	0
65	MR-8	RD-II	121	32.04	16.03	113	25,029	748	103	0
66	MR-8	RD-II	122	31.6	14.34	773	51,846	520	0	0
67	MR-8	RD-II	124	33.55	16.98	359	10,727	204	0	435
68	MR-12	CC	75	54.09	0.3762	140	1522	65	0	140
69	MR-12	CC	76	54.9	0.4391	0	1164	164	0	0
70	MR-12	CC	77	54.85	0.4401	532	1119	226	bdl	352
71	MR-12	CC	78	55.17	0.4364	598	1542	206	bdl	806
72	MR-12	CC	79	55.32	0.2264	517	899	74	bdl	240
73	MR-12	CC	80	55.24	0.1728	120	893	bdl	bdl	0
74	MR-12	CC	81	56.18	0.203	101	818	bdl	bdl	0
75	MR-12	CC	82	55.58	0.1677	86	1304	5	88	bdl.
76	MR-12	CC	83	55.74	0.0642	535	993	132	32	0
77	MR-12	CC	84	54.67	0.41	0	1021	122	bdl	0
78	MR-12	CC	85	54.18	0.4903	121	1120	98	bdl	bdl
79	MR-12	CC	86	55.49	0.2175	179	1325	0	bdl	734
80	MR-12	CC	87	55.92	0.3308	97	1349	79	bdl	bdl

Table 1. *Cont.*

Sr. No	Sample No	Phase	Point No	CaO Wt.%	MgO Wt.%	Na (ppm)	Fe (ppm)	Mn (ppm)	Zn (ppm)	Ba (ppm)
81	MR-6	Dedol.	4	54.31	0.6358	872	3170	308	0	301
82	MR-6	Dedol	5	55.13	0.5372	297	1576	143	0	542
83	MR-6	Dedol.	6	53.19	0.8163	617	2301	535	0	bdl
84	MR-6	Dedol	7	55.18	0.3626	243	3607	191	279	bdl
85	MR-6	Dedol.	8	55.2	0.3014	0	1769	133	0	bdl
86	MR-6	Dedol	9	55.89	0.3703	0	1321	0	0	bdl
87	MR-6	Dedol.	10	55.25	0.3096	266	637	185	200	bdl
88	MR-6	Dedol	11	54.36	0.3116	0	4180	222	0	bdl
89	MR-6	Dedol.	12	55.08	0.2513	bdl	1785	463	130	bdl
90	MR-6	Dedol	21	54.4	0.6553	0	2414	413	0	bdl
91	MR-6	Dedol.	22	53.78	0.7344	342	2203	150	76	bdl
92	MR-6	Dedol.	23	53.55	1.0515	264	4244	550	285	bdl
93	MR-6	Dedol.	24	54.16	0.4847	0	7684	263	0	bdl

(A)

(B)
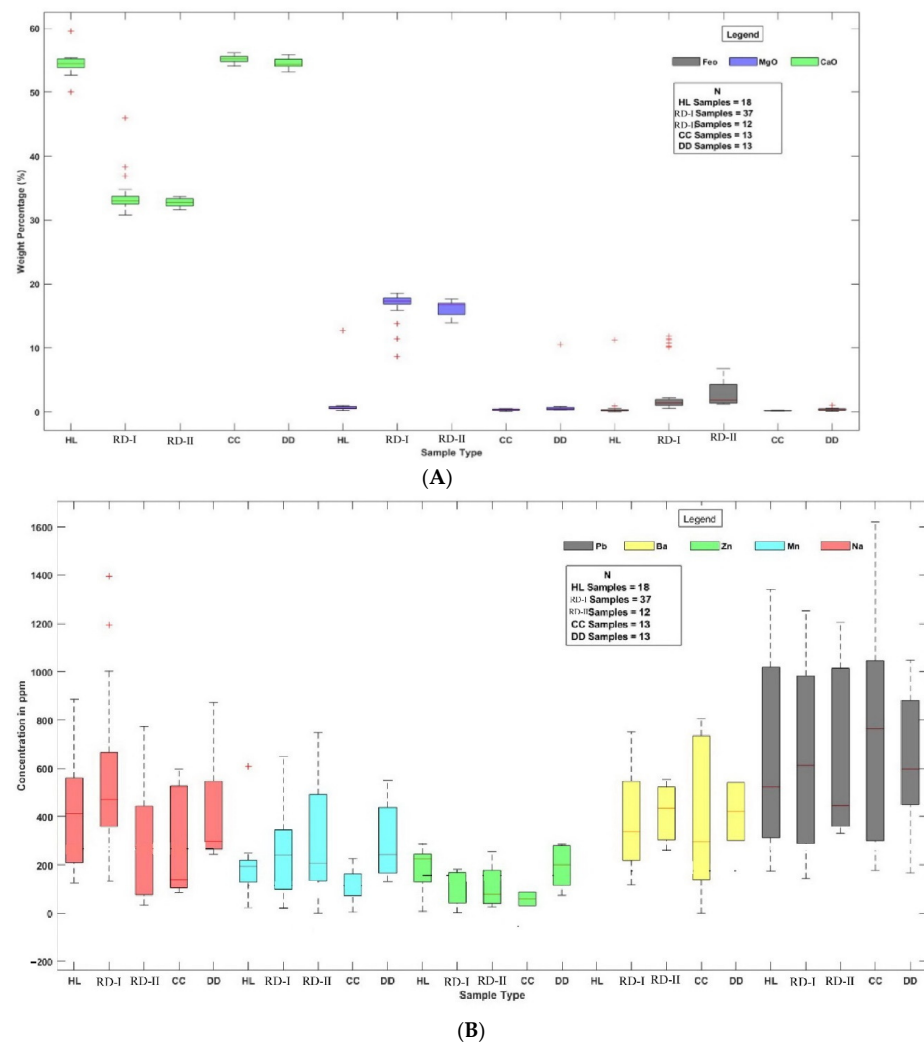
Figure 5. The box plot shows the concentration of major and trace elements of different dolomites and other diagenetic phases observed. (**A**) The box plot shows the concentration of major elements expressed in weight percentage. (**B**) The box plot shows the concentration of minor elements expressed in ppm. HL: host limestone, RD-I: matrix dolomite, RD-II: replacive dolomite, CC: fracture-filling calcite, DD: dedolomite.

The replacement dolomite cement (RD-II) has a CaO concentration ranging from 31.6 to 33.19 Wt.% $n = 12$, with an average of 31.15 Wt.% CaO. The MgO concentration ranges from 13.91 to 17.61 Wt.% ($n = 12$), with an average of 16.165 Wt.%. Na concentration ranges from (bdl to 773 ppm), with an average of 272 ppm. Fe concentration ranges from (9444 to 52,312 ppm), with an average of 22,810 ppm. Mn levels range from bdl to 748 ppm, with a mean of 308 ppm. Zn concentrations range from bdl to 255 ppm on average. The average Ba concentration ranges from bdl to 554 ppm (Figure 5A,B).

The fracture-filling calcite (CC) shows that it has a CaO concentration that ranges from 54.18 to 56.18 Wt.% ($n = 12$), with an average of 55.27 Wt.%. The MgO concentration ranges from 0.0642 to 0.49 Wt.% ($n = 12$), with an average of 0.30 Wt.%. Na concentration ranges from (bdl to 598 ppm), with an average of 244 ppm. Fe concentration ranges from (818 to 1542 ppm), with an average of 1143 ppm. The average Mn concentration ranges from bdl to 226 ppm. The Zn concentration is below the detection limit. Ba concentration ranges from bdl to 806 ppm, with an average of 227 ppm (Figure 5A,B).

The dedolomite (DD) shows that it has a CaO concentration ranging from 53.19 to 55.89 wt.% ($n = 13$), with an average of 54.57 wt.% CaO. The MgO concentration ranges from 0.25 to 1.05 wt.% ($n = 13$), with an average of 0.52 wt.%. Na concentrations range from bdl to 872 ppm; the average for $n = 13$ is 240 ppm. Fe concentrations range from 637 to 7684 ppm, with an average of 2837 ppm ($n = 13$). Mn concentrations range from bdl to 550 ppm; the average for $n = 13$ is 273 ppm. The concentration of Zn ranges from bdl to 285 ppm; $n = 13$, average (bdl). Ba concentrations ranged from bdl to 542 ppm on average ($n = 13$) (Figure 5A,B).

To determine the concentration of various elements, transects of EMP equipped with WDX of different diagenetic phases, such as matrix and replacive phases of dolomite, were performed (Figure 6). It is interesting to note that the Fe concentration of matrix dolomite (RD-I) is relatively less than that of replacive dolomite (RD-II). The Na concentration of matrix dolomite (RD-I) is relatively higher than that of replacement dolomite (RD-II). The Mn concentration of replacive dolomite (RD-II) is relatively higher than that of matrix dolomite (RD-I) (Figure 6).

4.2.2. Stable C and O Isotopic Studies

Fifty-seven samples of dolomite and calcite phases were selected from four different sections for the stable isotope analysis. The $\delta^{13}C$ & $\delta^{18}O$ values of various dolomite and calcite phases are given in the table (Table 2). The results are compared to the signature of the North West Tethys Ocean Jurassic carbonates taken from Al-Mojel et al. [50] (Figure 7).

The unaltered micrite matrix shows a $\delta^{18}O$ value of $-0.44‰$ V-PDB ($n = 1$) and a $\delta^{13}C$ value of $-2.6‰$ V-PDB ($n = 1$). The $\delta^{18}O$ values of host limestone range from $-6.66‰$ to $-4.31‰$ V-PDB ($n = 15$), and $\delta^{13}C$ values range from $-0.11‰$ to $2.07‰$ V-PDB ($n = 15$). The values show the depletion trend in oxygen isotope values when compared with the signature of the Jurassic marine carbonates, while the carbon isotopic values are consistent with the same signature (Dera et al., 2011; Figure 7). The $\delta^{18}O$ values of matrix dolomite (RD-I) range from $-2.94‰$ to $-0.99‰$ V-PDB ($n = 8$), and the $\delta^{13}C$ ranges from $0.53‰$ to $3.19‰$ V-PDB ($n = 8$). The oxygen and carbon isotopic values of RD-I fall within the Jurassic marine signature (Dera et al., 2011; Figure 7). The patchy replacive dolomite (RD-II) yielded $\delta^{18}O$ values ranging from $-6.20‰$ to $-4.12‰$ V-PDB ($n = 13$) and $\delta^{13}C$ values ranging from $-1.3‰$ to $1.81‰$ V-PDB ($n = 13$).

The $\delta^{18}O$ values of saddle dolomite range from $-7.64‰$ to $-6.65‰$ V-PDB ($n = 04$) and $\delta^{13}C$ values ranges from ($1.39‰$ to $2.34‰$ V-PDB; $n = 04$). The $\delta^{18}O$ values of fracture-filling calcite (CC) range from $-12.32‰$ to $-8.61‰$ V-PDB; $n = 4$; and $\delta^{13}C$ values range from $-0.08‰$ to $-0.05‰$ V-PDB; $n = 4$ showing the highest depletion trend in terms of oxygen isotopes, while the carbon isotope values fall within Jurassic marine signatures (Figure 7). The $\delta^{18}O$ value of de-dolomites ranges from $-8.32‰$ to $-6.78‰$ V-PDB; $n = 12$ and $\delta^{13}C$ value ranges from $-5.01‰$ to $-0.45‰$ V-PDB; $n = 12$.
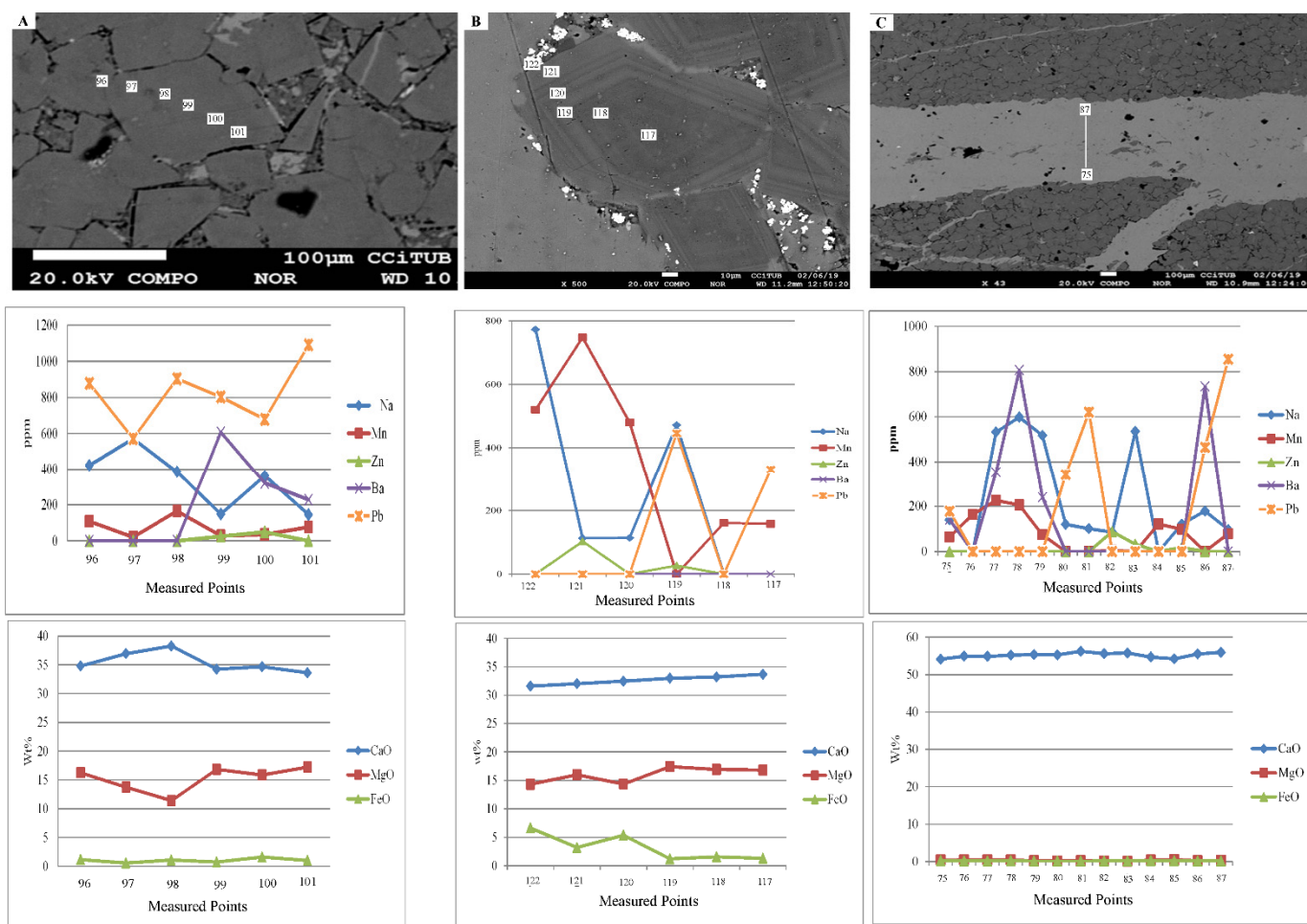
Figure 6. Microprobe profile analysis of the different types of dolomite and calcite phases. (**A**) Microprobe image shows the detailed profile of matrix dolomite (RD-I). The profile given below shows the trace element composition of a particular phase. Note that the Na concentration is relatively high in this phase. (**B**) Shows the detailed profile of replacive dolomite (RD-II). The profile given below shows the trace element composition of that particular phase. Note that the Na concentration is relatively high in this phase. (**C**) Microprobe image showing the detailed profile of fracture-filling calcite cement (CC). The profile given below shows the trace element composition of a particular phase. No particular trend is observed here.

Table 2. Stable ($\delta^{18}O$ and $\delta^{13}C$) and radiogenic $^{87}Sr/^{86}Sr$ isotope data of the studied Samana Suk Formation.

Sr. No	Sample Code.	Phase	$\delta^{13}C$ ‰ (V-PDB)	$\delta^{18}O$ ‰ (V-PDB)	$^{87}Sr/^{86}Sr$ ($\pm\sigma$)
1	PM-24-A	Micritic Matrix	2.59	−0.44	0.707718
2	PM-5A	Limestone	−0.11	−5.99	
3	PM-28-A	Limestone	1.44	−5.16	
4	PM-33-A	Limestone	0.97	−5.65	
5	PM-44-A	Limestone	0.76	−5.87	
6	PM-77A1	Limestone	1.78	−5.61	
7	PM-77A2	Limestone	1.83	−5.67	
8	BG-2A	Limestone	0.94	−4.96	
9	BG-15A	Limestone	1.02	−5.57	
10	KS-14	Rudist Shells/ Limestone	1.28	−4.31	

Table 2. *Cont.*

| Sr. No	Sample Code.	Phase	$\delta^{13}C$ ‰ (V-PDB)	$\delta^{18}O$ ‰ (V-PDB)	$^{87}Sr/^{86}Sr$ ($\pm\sigma$)
11	KS-15A	Limestone	1.58	−5.04	
12	KS-16A	Limestone	1.36	−6.01	
13	MR-12A	Limestone	1.58	−5.67	
14	MR-13A	Limestone	1.56	−5.65	
15	MR-26A	Limestone	1.74	−4.79	
16	MR-26B	Limestone	2.07	−4.80	
17	PM-10A	RD-I	1.05	−2.34	
18	PM-10B	RD-I	1.15	−2.94	
19	PM-23C	RD-I	3.19	−0.99	0.707703
20	PM-33-B	RD-I	0.53	−2.60	
21	BG-15B	RD-I	1.29	−3.60	
22	BG-22A	RD-I	1.48	−1.92	0.707952
23	MR-12B	RD-I	2.52	−1.31	0.707972
24	KS-9	RD-I	1.32	1.8	
25	PM-20A	RD-II	1.81	−4.37	
26	PM-24B	RD-II	1.59	−4.68	
27	PM-63-A	RD-II	−1.3	−6.41	
28	PM-77B	RD-II	−0.35	−5.37	0.708839
29	PM-77B1	RD-II	1.26	−5.15	
30	PM-77B2	RD-II	0.47	−4.68	
31	PM-77B3	RD-II	0.51	−4.69	
32	BG-6A	RD-II	0.47	−4.95	
33	BG-8A	RD-II	0.12	−5.99	0.70889
34	BG-9B	RD-II	0.97	−6.21	
35	BG-12A	RD-II	−0.69	−5.12	
36	KS-17A	RD-II	1.73	−4.122	
37	KS-18B	RD-II	1.03	−6.26	
38	PM-23A	SD	1.85	−6.88	
39	PM-49A	SD	1.83	−7.64	
40	MR-2A	SD	1.39	−7.00	
41	MR-37A	SD	2.34	−6.65	0.710747
42	BG-12B	CC	1.36	−9.38	
43	KS-15B	CC	1.34	−12.32	0.709061
44	KS-17B	CC	0.90	−8.97	
45	MR-2B	CC	0.23	−8.61	
46	PM-2	Dedol.	−2.36	−7.69	
47	PM-7A	Dedol.	−2.55	−6.57	
48	PM-44-B	Dedol.	−2.64	−8.34	
49	PM-79A	Dedol.	−3.45	−7.15	
50	PM-83A	Dedol.	−5.01	−7.57	
51	PM-85A	Dedol.	−0.06	−7.35	
52	PM-86	Dedol.	−2.06	−8.32	
53	BG-5B	Dedol.	−1.32	−5.74	
54	BG-7A	Dedol.	−0.45	−7.04	
55	KS-1	Dedol	−1.4	−7.7	
56	KS-15C	Dedol	−1.80	−6.79	
57	KS-16B	Dedol.	1.36	6.78	
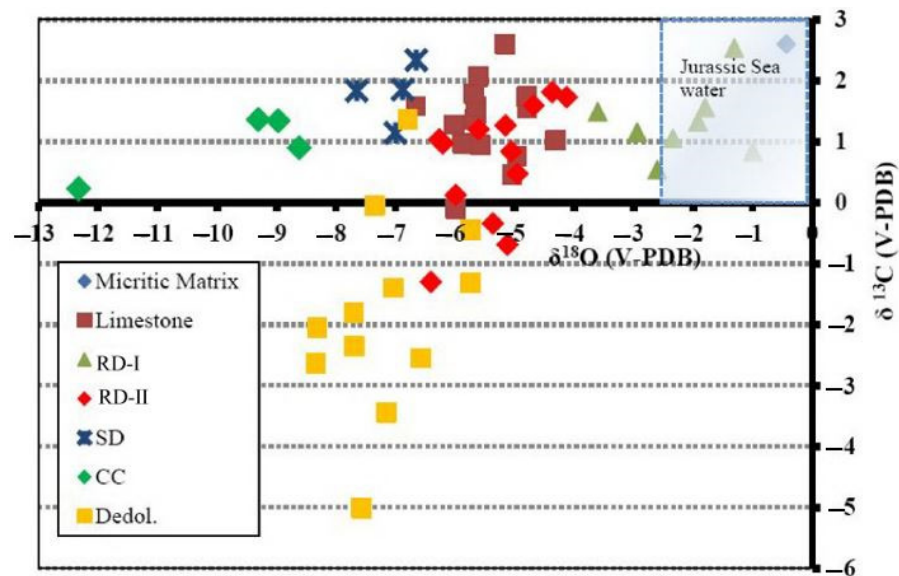
Figure 7. Cross-plot between carbon and oxygen isotopes. The blue box indicates the Jurassic marine seawater signatures of NW Tethys, compiled after Al-Mojel, Dera, Razin, and Le Nindre [50]. RD-I: matrix dolomite, RDII, replacive dolomite, SD: saddle dolomite, CC: fracture-filling calcite cement, Dedol: dedolomite.

4.2.3. Radiogenic Sr Isotopes

The strontium isotope ratio ($^{87}Sr/^{86}Sr$) was measured on the 8 samples representing different phases of dolomite and calcite (Table 2). The lowest $^{87}Sr/^{86}Sr$ isotope ratios were measured in the micritic limestone matrix sample (0.707718; *n* = 1), which is in agreement with the reported value of Jurassic seawater [51] (Figure 8A). The matrix dolomite (RD-I) has an $^{87}Sr/^{86}Sr$ isotope ratio ranging between 0.707703–0.707972 (*n* = 3) (Table 2; Figure 8A). The patchy replacive dolomite (RD-II) has an $^{87}Sr/^{86}Sr$ isotope ratio ranging between 0.708839 and 0.708890 (*n* = 2) (Table 2; Figure 8A). The saddle dolomite (SD) has an $^{87}Sr/^{86}Sr$ isotope ratio of 0.710747 (*n* = 1) (Table 2; Figure 8A). The fracture-filling calcite has an $^{87}Sr/^{86}Sr$ isotope ratio of 0.709061 (*n* = 1) (Table 2; Figure 8A).
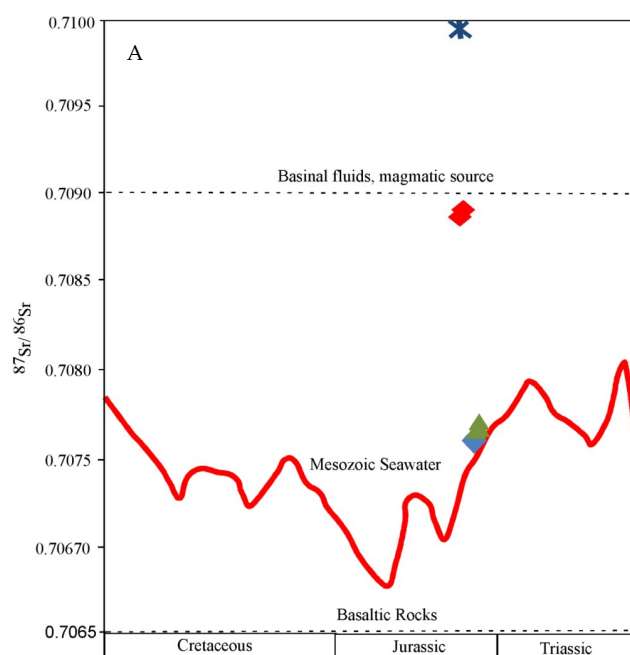
Figure 8. *Cont.*
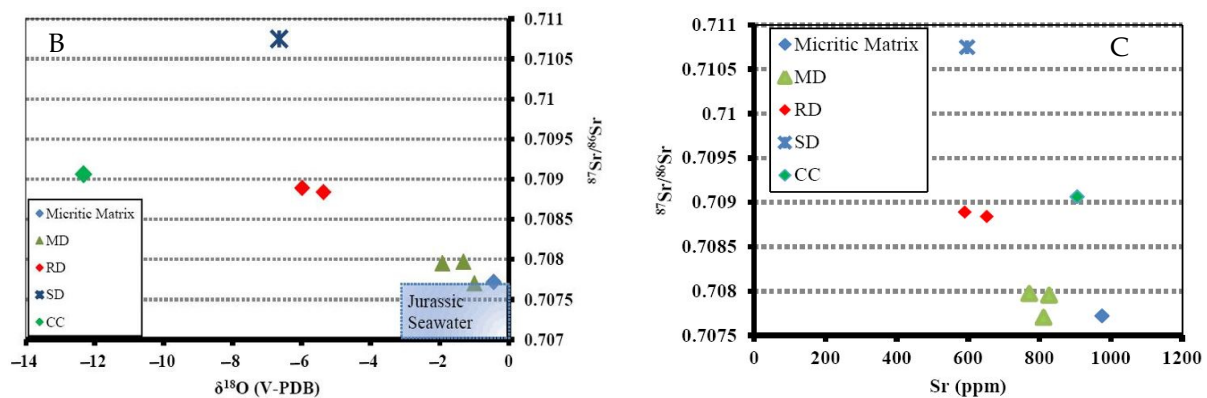
Figure 8. (**A**) $^{87}Sr/^{86}Sr$ curve for the seawater of the Mesozoic era (redrawn after McArthur, Howarth, and Shields [51]). (**B**). Cross-plot between $\delta^{18}O$ values versus $^{87}Sr/^{86}Sr$ for the different diagenetic phases. The blue box indicates the Jurassic marine seawater signatures of NW Tethys compiled by Al-Mojel, Dera, Razin, and Le Nindre [50]. (**C**). There is a cross-plot between Sr concentration and $^{87}Sr/^{86}Sr$ of different dolomite and calcite phases. RD-I: matrix dolomite, RD-II: replacive dolomite, SD: saddle dolomite, CC: fracture-filling dolomite.

Combining the $^{87}Sr/^{86}Sr$ data with the $\delta^{18}O$ data represents different sample groups very well (Figure 8B). The matrix dolomites (RD-I) are characterized by relatively enriched oxygen and relatively un-radiogenic Sr isotope composition compared to the Jurassic seawater, while the patchy replacive dolomites (RD-II) show more depleted oxygen and more radiogenic Sr isotope composition (Figure 8B) In terms of $^{87}Sr/^{86}Sr$ ratio, saddle dolomite is the most radiogenic, far from the Jurassic seawater signature (Figure 8B). The fracture-filling calcite has the most depleted $\delta^{18}O$ signatures and is also radiogenic in terms of Sr isotope composition (Figure 8B).

4.2.4. Sr Concentration

The Sr concentration of all observed dolomite phases is determined along with the Sr isotope concentration. The observed Sr concentration is also plotted against an $^{87}Sr/^{86}Sr$ ratio, which shows that the Sr concentration of micrite matrix (976 ppm; *n* = 1) and matrix dolomite (RD-I) have (772 to 812 ppm; *n* = 3) generally higher concentrations of Sr and less radiogenic Sr isotope ratios. The replacive dolomite (RD-II) has a relatively low Sr concentration (591 to 653 ppm; *n* = 2) and a higher radiogenic Sr isotope ratio (Figure 8C). The saddle dolomite (SD) has a low Sr concentration of 598 ppm (Figure 8C) and the highest radiogenic Sr isotope ratio. The fracture-filling calcite has a Sr concentration of 906 ppm and high radiogenic Sr isotope values (Figure 8C).

4.3. Fluid Inclusion Analysis

Fluid inclusion studies were carried out on 36 isolated two-phase fluid inclusions (Table 3). Matrix dolomites (RD-I) and replacive dolomite (RD-II) are dark-colored and very small crystal sizes; therefore, they are excluded from the fluid inclusion analysis. By contrast, the saddle dolomite (SD) and fracture-filling calcite (CC) contain measurable biphasic fluid inclusions (Figure 9). The size of fluid inclusions varies from 5 to 8 μm in saddle dolomite to 8–10 μm in fracture-filling calcite (Figure 9). In saddle dolomite, the primary fluid inclusions are mostly concentrated along the rims of crystals (Figure 9A). In the calcites, fluid inclusions are concentrated along the crystal growth zones and thus are interpreted as of primary origin (Figure 9D–F). In calcites, trails of fluid inclusions along the fracture zone are also present with ambiguous homogenization temperatures, but they are excluded from the analysis. Most of the fluid inclusions have very inconsistent long-range homogenization temperature and salinity, which indicates a possibility of thermal re-equilibration effect of the crystals (Figure 10A, B). The homogenization temperature of the saddle dolomite ranges between 102.8 and 186 °C (*n* = 21; average 132.2 °C), with the

highest frequency interval ranging from 100 to 131 °C (Figure 10A). The homogenization temperature of fracture-filling calcite (CC) ranges between 68.0 and 98.4 °C (*n* = 15; average 84.8 °C) (Figure 10B). No pressure correction is applied to the homogenization temperature as the burial depth of these phases is only approximately calculated from the burial history curve of the borehole present in the vicinity.

Table 3. Fluid inclusion data for dolomites and fracture-filled calcite samples of the Samana Suk Formation.

Sr. No	Sample No	Phase	T_h	T_{mi}	Eq. Wt.% NaCl
1	MR-37	Saddle Dolomite(SD)	118.6	−12.0	16.0
2	MR-37	Saddle Dolomite(SD)	119.6	−11.0	15.0
3	MR-37	Saddle Dolomite(SD)	121.0	−8.0	11.7
4	MR-37	Saddle Dolomite(SD)	122.5	−11.0	15.0
5	MR-37	Saddle Dolomite(SD)	110.4	−16.0	19.4
6	MR-37	Saddle Dolomite(SD)	108.4	−15.0	18.6
7	MR-37	Saddle Dolomite(SD)	119.7	−14.0	17.8
8	MR-37	Saddle Dolomite(SD)	131.7	−15.0	18.6
9	MR-37	Saddle Dolomite(SD)	137.6	−15.0	18.6
10	MR-37	Saddle Dolomite(SD)	125.4	−13.0	16.9
11	MR-37	Saddle Dolomite(SD)	127.6	−15.5	19.0
12	MR-21	Saddle Dolomite(SD)	122.8	−14.0	17.8
13	MR-37	Saddle Dolomite(SD)	124.8	−12.0	16.0
14	MR-37	Saddle Dolomite(SD)	121.0	−9.0	12.8
15	MR-37	Saddle Dolomite(SD)	126.0	−13.0	16.9
16	MR-37	Saddle Dolomite(SD)	129.8	−15.0	18.6
17	MR-37	Saddle Dolomite(SD)	102.8	−14.0	17.8
18	MR-37	Saddle Dolomite(SD)	180.5	−15.0	18.6
19	MR-37	Saddle Dolomite(SD)	186.0	−13.0	16.9
20	MR-37	Saddle Dolomite(SD)	169.0	−15.0	18.6
21	MR-37	Saddle Dolomite(SD)	171.0	−15.0	18.6
22	KS-15	Hydrothermal Calcite	92.4	−8.0	11.7
23	KS-15	Hydrothermal Calcite	92.6		−
24	KS-15	Hydrothermal Calcite	93.8	−8.4	12.2
25	KS-15	Hydrothermal Calcite	98.4	−9.2	13.1
26	KS-15	Hydrothermal Calcite	86.4	−6.5	9.9
27	KS-15	Hydrothermal Calcite	89.5	−7.9	11.6
28	KS-15	Hydrothermal Calcite	82.4	−5.9	9.1
29	KS-15	Hydrothermal Calcite	85.9	−6.2	9.5
30	KS-15	Hydrothermal Calcite	88.7	−8.3	12.0
31	KS-15	Hydrothermal Calcite	87.8	−8.1	11.8
32	KS-15	Hydrothermal Calcite	78.6	−5.8	8.9
33	KS-15	Hydrothermal Calcite	73.5	−4.8	7.6
34	KS-15	Hydrothermal Calcite	77.9	−5.5	8.5
35	KS-15	Hydrothermal Calcite	76.6	−5.8	8.9
36	KS-15	Hydrothermal Calcite	68.0	−4.3	6.9

As most of the inclusions are small in size, low-temperature phase changes could not be identified. The only measurable reading of both saddle dolomite and vein calcite is the last ice melting (T_{mi}). The T_{mi} of saddle dolomite ranges from −15.5 °C to −8.0 °C (average −13.4 °C), and fracture-filling calcite between −9.2 °C and −4.3 °C (average −6.8 °C) (Figure 10C; Table 3). The T_{mi} values are used to calculate the salinity of fluids by using the relationship of Bodnar (1993). The salinity of saddle dolomite (SD) ranges between 11.7 and 19.4 eq. wt.% NaCl (average 17.1 eq. wt.% NaCl), and fracture-filling calcite between 6.9 and 13.1 eq. wt.% NaCl (average 10.1 eq. wt.% NaCl) (Figure 10C; Table 3).
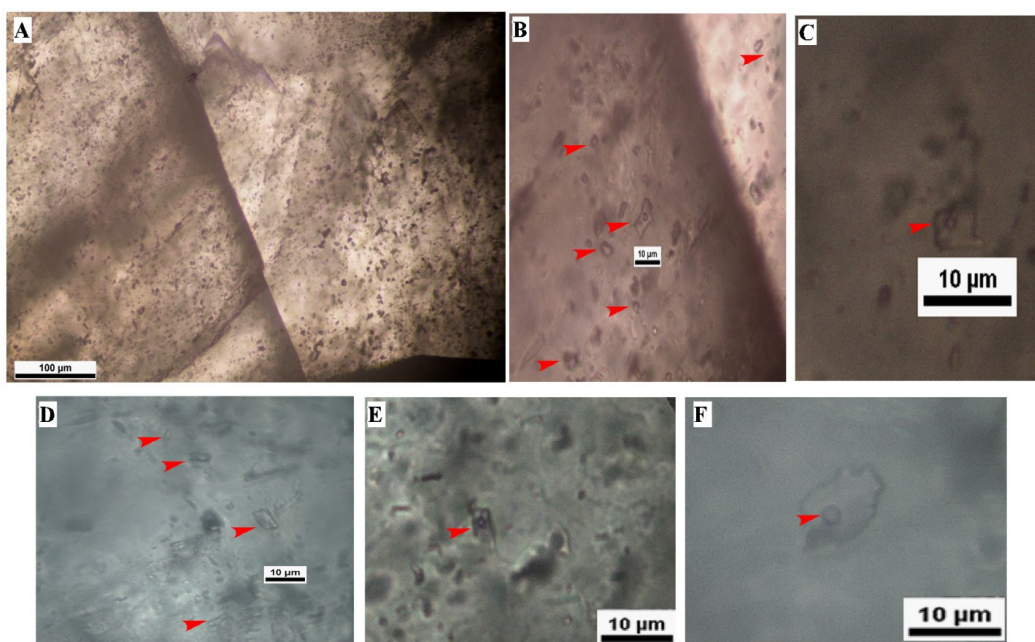
Figure 9. (**A**) Petrographic characteristics of biphasic fluid inclusions (**A**–**C**). The inclusions are present in the saddle dolomite and (**D**–**F**) fracture-filling calcite. The red arrow shows the position of the gas bubble.
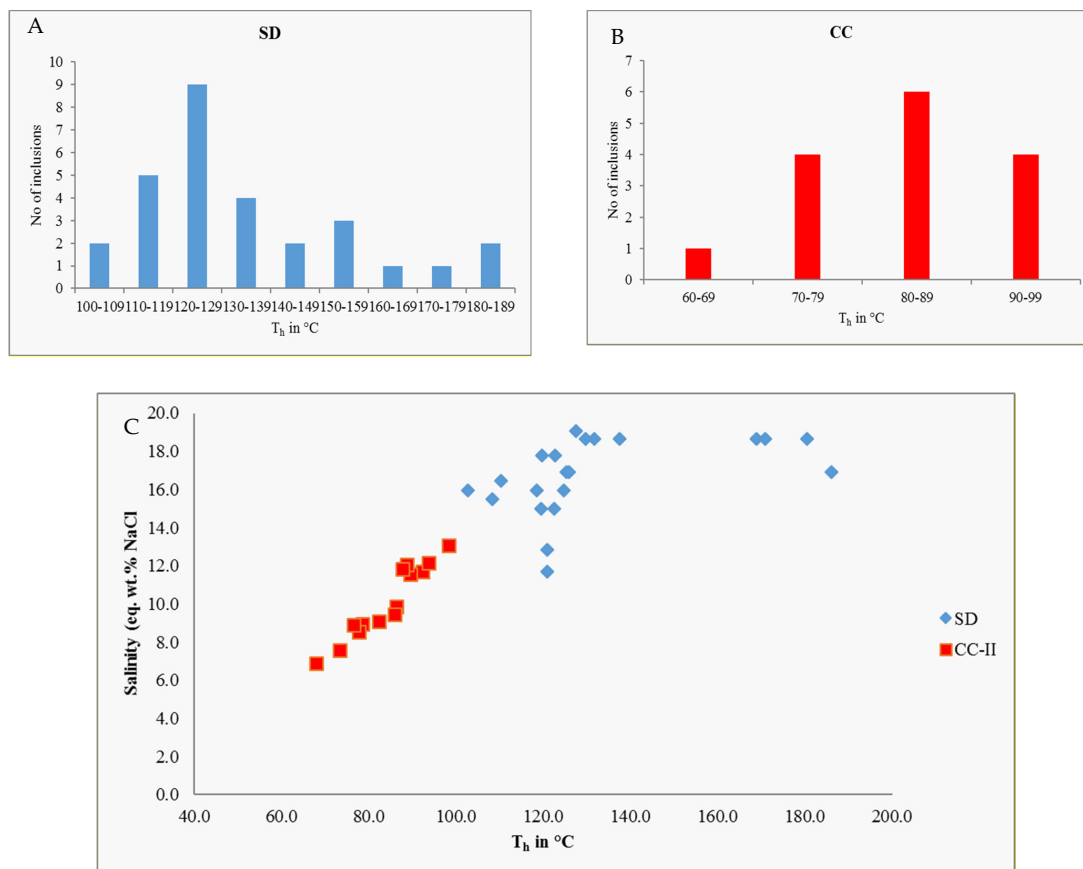

Figure 10. Fluid inclusion data of the saddle dolomite and fracture-filling calcite. (**A**) histogram showing the homogenization temperature of saddle dolomite. (**B**) histogram showing the homogenization temperature of fracture-filling calcite. (**C**) homogenization temperature versus salinity data of saddle dolomite (SD) and fracture-filling calcite (CC).

5. Discussion

5.1. Origin of Dolomite Phases

Field and analytical results revealed that two distinct dolomitization episodes affected the platform carbonates of the Samana Suk Formation.

Field evidence indicates that matrix dolostone (RD-I) occurs as strata-bound units. The dolomite bodies, which are formed during or soon after deposition, may retain geometries similar to the original depositional geobodies; hence they are often called stratabound or stratiform dolomites (Figure 3D). Patchy replacive dolostone (RD-II) field geometry shows that they tend to form along weak planes (fractures, stylolites, burrow-related void spaces, and parallel bedding planes) (Figure 3C–H). Field observations show a sharp contact between limestone and dolomite units, suggesting a late diagenetic origin of the replacive dolomites. The host limestone and dolomite (RD-I, RD-II) are cross-cut by the fracture-filling calcite veins, suggesting the late origin of the latter (Figure 3C).

The non-luminescent nature of matrix dolomite (RD-I) and its fine-grained crystals indicate that it was formed at a low temperature during an early stage of diagenesis, as suggested by various workers, e.g., Sibley and Gregg [42], Gregg and Shelton [52], Warren [2], Machel [3], Zheng et al. [53], and Van Lith et al. [54] (Figure 4A,B). The replacive dolomite showing planer textures with concentric compositional zoning is indicative of hydrothermal origin [2,52].

Geochemically, the relative abundance of major and trace elements in dolomites gives clues about the dolomitization process [5,9]. The Na is the mobile element during diagenesis, which makes an analytical assessment based on this element more unreliable [55]. However, it is suggested that early diagenetic dolomites have higher Na content than late diagenetic dolomites [56–58]. The Na concentration of matrix dolomite of the Samana Suk Formation is relatively higher than the late replacive dolomite (RD-II) cement, although no clear trend is observed (Figures 6B and 7).

The iron and manganese content usually tends to increase during the diagenesis of carbonates [59]. Therefore, early dolomites precipitated in relatively oxidizing conditions have low iron and manganese concentrations, while the burial dolomites tend to have higher iron and manganese. The same trend is observed in the dolomites reported from the Samana Suk Formation, where matrix dolomites show a low content of Fe and Mn, which is consistent with a formation from near-surface processes, while the replacive dolomites show a high content of Fe and Mn, which is consistent with a formation from burial processes (Figure 6B). During later stages related to uplift, these elements tend to reduce in fracture-filling calcite and dedolomite, indicating uplift of the rock units. It has been documented that zinc accelerates the dolomitization process [10]. The observed concentration of zinc in the dolomites (RD-I, RD-II) of the Samana Suk Formation is significantly higher than the limestone (Figure 6B). It has been documented that the Ba element is only incorporated into the carbonate lattice at high temperatures [60]. The Ba concentration ranges from below the detection limit (bdl) to 806 ppm (Table 1). As a result, the high Ba content of replacive dolomite and fracture-filling calcite suggests a hydrothermal origin.

The analysis of ^{87}Sr/^{86}Sr values on marine carbonates reveals that the ratio changed systematically in open oceans during the Phanerozoic period [51,61]. According to Allen and Wiggins (1993), the dolomites, which are derived from the subsurface brines, have an elevated ^{87}Sr/^{86}Sr ratio. Moreover, prolonged fluid–rock interaction with the subsurface fluids usually results in a more enriched Sr ratio [7,62–66]. The dolomites of the Samana Suk Formation are clustered into three main groups compared to the Jurassic marine carbonate signature: (i) matrix dolomite and host limestone both have a similar ^{87}Sr/^{86}Sr ratio; (ii) replacive dolomite with a ratio of 0.7092–0.7101 that is significantly higher than the ratio in the limestone (0.7077) suggests fluid interaction with a source of radiogenic strontium. The possible candidate for providing the radiogenic strontium could be the sandstone of the Early Jurassic Datta Formation, stratigraphically underlying the Samana Suk Formation. As reported by Iqbal et al. [67], the Datta Formation is a feldspathic sandstone with laterite and bauxite horizons. The radiogenic strontium was possibly leached from these feldspars.

Analysis of the cross plot between δ^{13}C and δ^{18}O of diagenetic phases of dolomite and calcite follows the inverted J pattern representing the fluid–rock interaction at various stages of diagenesis [68,69] (Figure 7).

Diagenesis driven by the influence of meteoric water yields carbonates with negative δ^{13}C values [70]. However, positive δ^{13}C values of limestone and dolomite phases of the Samana Suk Formation indicate that the diagenetic processes, including dolomitization, occurred in an open system; however, there was no influence of meteoric water before dolomitization. However, during the later stages, the study area was subjected to uplift because of the Himalayan orogeny. This caused a negative δ^{13} value of replacive dolomites due to dedolomitization by meteoric influx, as revealed by the petrographic and stable isotopic analysis [71] (Figures 4G,H and 7).

The δ^{18}O values of dolomites reflect the isotopic composition and temperature of dolomitizing fluids [72]. Dolomites, which are directly precipitated from seawater, have about 0–3 δ^{18}O values [63]. The dolomites of the Samana Suk Formation show bimodal distribution. The δ^{18}O value of matrix dolomite ranges from −3.6‰ to −0.99‰ V-PDB, which is in agreement with the Jurassic marine signatures of the Tethys Ocean [8]. The δ^{18}O value of limestone ranges from −6.01‰ to −4.79‰ V-PDB showing more depleted signatures than Jurassic marine waters. The resultant isotopic values of limestone suggest buffering of host limestone by the heat source (Figure 7). The δ^{18}O value of replacive dolomite ranges from −6.41‰ to −4.37‰ V-PDB, suggesting the elevated temperature range of replacive dolomitization as compared to the host limestone and matrix dolomite. The V-PDB value of saddle dolomite ranges from −7.64‰ to −6.65‰, indicating that it is formed at high temperatures.

In order to determine the δ^{18}O (‰ SMOW) fluid composition of RD-I, RD-II, and SD, the values of δ^{18}O (V-PDB) were plotted against the T_h by using the fractionation equation of land [58]. This plot shows that the inferred δ^{18}O (‰ SMOW) fluid values of matrix dolomite (RD-I) range between −4‰ and 2‰ (V-SMOW), showing their origin from marine waters (Figure 11A). The δ^{18}O (V-SMOW) fluid values of replacive dolomite (RD-II) range between 3‰ and 6‰ enriched than the marine waters signature, indicating the fluid origin from a hydrothermal source of probably magmatic or basement-derived rocks (Figure 11A). The δ^{18}O (V-SMOW) fluid values of saddle dolomites (SD) range between 4‰ and 12‰ enriched than the marine waters signature indicating the fluid origin from a hydrothermal source of probably magmatic or basement-derived rocks [73] (Figure 11A). In the case of fracture filling, the calcite (CC) fractionation equation of Friedman and O'Neil [74] is used. The δ^{18}O (V-SMOW) fluid values of fracture-filling calcite (CC) range from −4 to +4, slightly enriched than the marine waters signature, indicating a fluid origin from lithologies most likely derived from basement rocks [53] (Figure 11B).

The homogenization temperature of the saddle dolomite ranges from 102.8 to 186 °C, with an average of 132.2 °C, suggesting a burial depth of 3.5 to 4 km assuming a surface temperature of 25 °C and geothermal gradient of 30 °C/Km. The studied formation might have been subjected to that particular burial depth as depicted from the burial history plot of the adjacent borehole (Figure 12). This burial might have caused the squeezing of the underlying Datta Sandstone unit. In addition, intense tectonic activity during the Cretaceous might have produced the thermal convective circulation system for delivering Mg in appreciable amounts to produce replacive and saddle dolomitization. The fractures present due to tectonic activity provided pathways for the circulation of these hydrothermal fluids. The possible heat source provided to the thermal convective system. Taking the tectonic activity of the area into account, the Indian plate remained on the hotspot during the Cretaceous and Upper Paleocene, which resulted in the outpouring of extensive flood basalts in major parts of the Indian plate. The studied formation was deposited before this time and might have provided sufficient hydrothermal fluids. The hydrothermal event can be corroborated by the hotspot activity over the Indian plate [75–77].
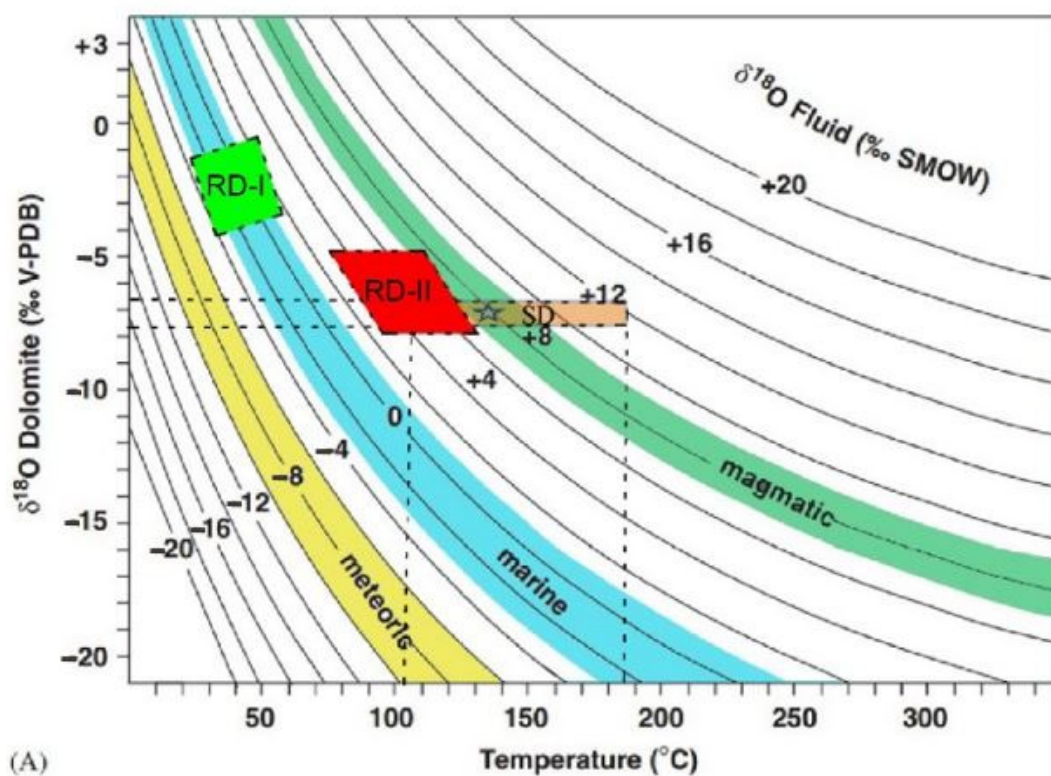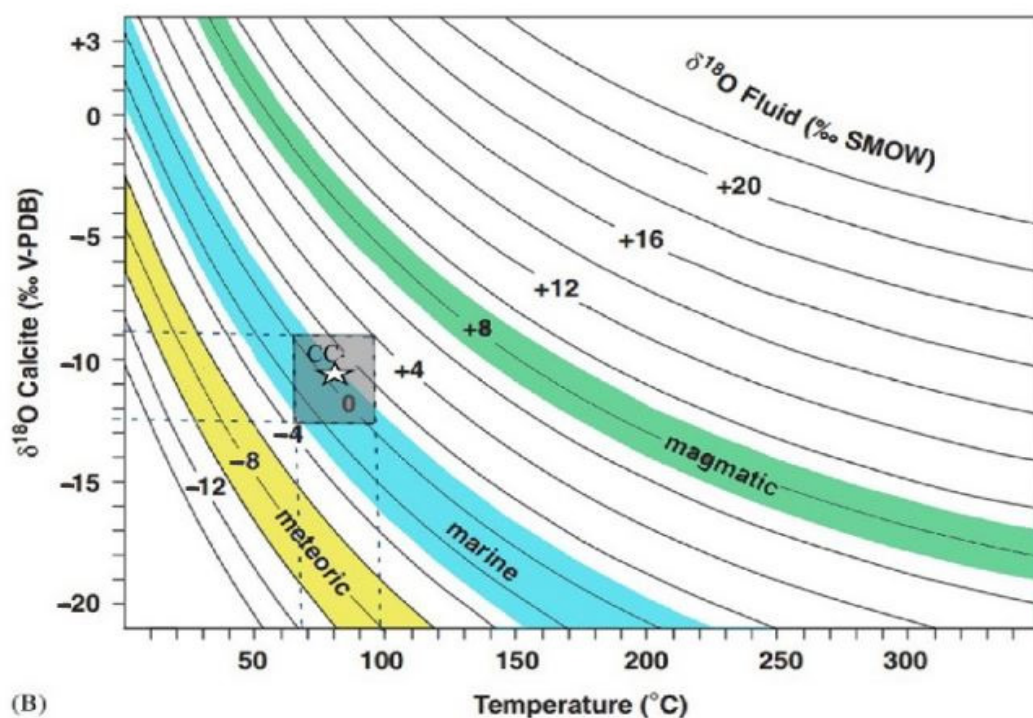
Figure 11. Homogenization temperature versus O isotopic composition of the carbonate phases analyzed: (**A**) The $\delta^{18}O$ of the fluid in equilibrium with matrix dolomite (RD-I), replacive dolomite (RD-II), and saddle dolomite (SD) is calculated using the fractionation equation of land [58]. (**B**) The $\delta^{18}O$ of the fluid in equilibrium with fracture-filling calcite (CC) is calculated using the fractionation equation of Friedman and O'Neil [74].
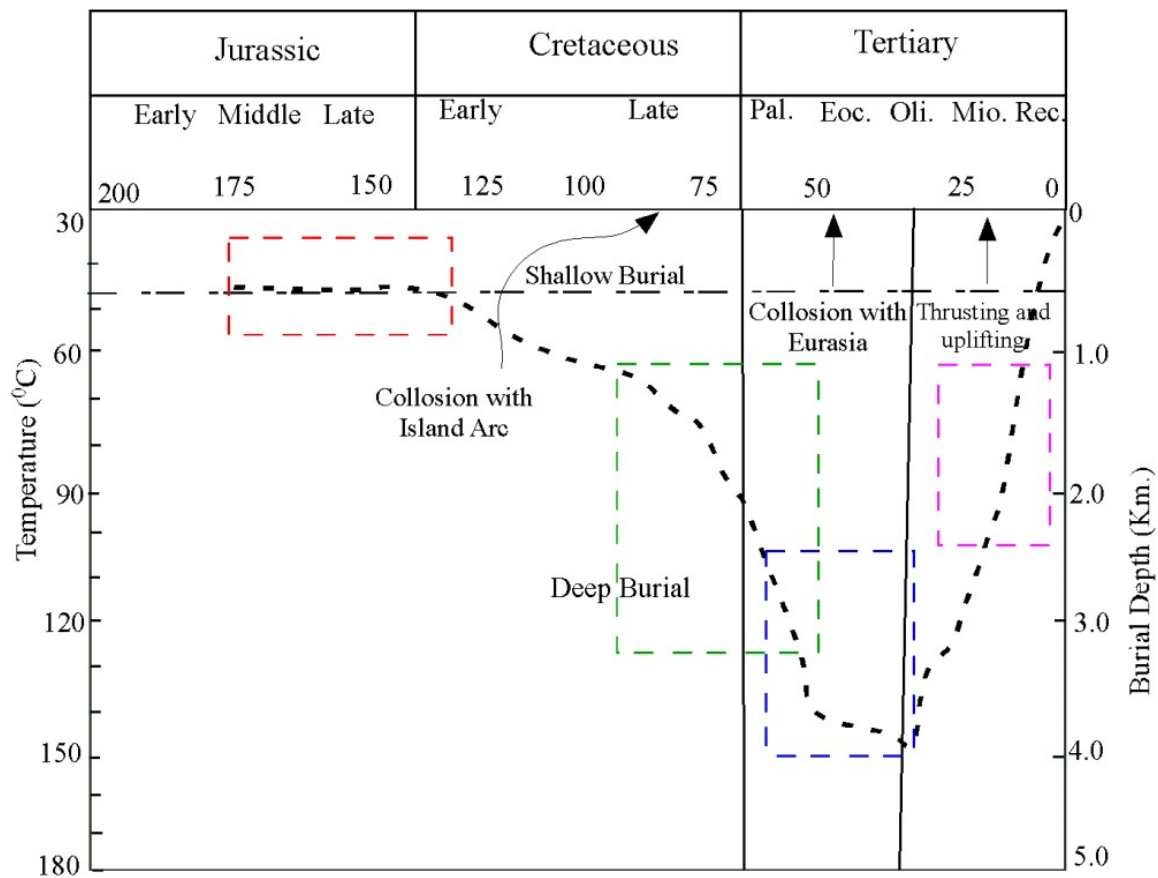
Figure 12. The burial history plot of the Jurassic succession of the Indus basin was modified after [19]). The curve is constructed by assuming a surface temperature of 30 °C and a geothermal gradient of 30 °C. The presumable diagenetic processes are marked with dotted rectangles. Red: matrix dolomite (RD-I), Green: replacive dolomite (RD-II), blue: saddle dolomite (SD), Pink: fracture-filling calcite (CC).

Fracture-filling calcite (CC) is possibly related to the hot waters that originated because of the high-rising orogenic belt. This was supported by the cross-cutting relationship as observed in the field and petrographic studies (Figures 3G,H and 4C). The dolomitization of the replacive and saddle dolomites is probably caused by the interaction of the meteoric fluids with dolomites [10,78]. This was supported by the fact that the de-dolomites have a mottled appearance under CL and a negative δ^{13} C trend (Figures 4G,H and 7).

5.2. Origin of Dolomitizing Fluids

To understand the origin of dolomitizing fluids, it is necessary to evaluate the potential source of Mg for the significant volume of the succession replaced by dolostones [2,3,6,58]. Field data indicate that 40 to 50% of the host carbonates have been dolomitized in the Samana Suk Formation.

As discussed earlier, two genetically distinct dolomite geobodies are identified, so their dolomitizing fluids should be from distinct sources which have played a role in the dolomitization of the Samana Suk Formation.

In the case of matrix dolomite occurring as stratiform units (Figure 3D), the major source of Mg is seawater [79,80]. The isotopic data presented here are consistent with the Jurassic seawater (Figures 7 and 8).

Paleogeographically, during the middle Toarcian to early Bajocian Indian plate, was located in the 30° S in the southern subtropical arid belt with mean annual precipitation of less than 2 cm per month [31,34,39] (Figure 13A). A similar environment of deposition is documented in southern Tibet [81]. The presence of burrows, fenestral pores, cauliflower

calcite, and herringbone cross stratification indicates a peritidal to intertidal environment with restricted water circulation [39]. In such environments, evaporation results in the precipitation of gypsum nodules, which are later psodumorphosed into cauliflower-shaped calcites as observed in the formation [82]. Such mesohaline conditions favor the formation of evaporative dolomite as stratabound units due to refluxing brines [3,80]. The less depleted $\delta^{18}O$ and less radiogenic $^{87}Sr/^{86}Sr$ ratio support the formation of stratiform matrix dolomites.
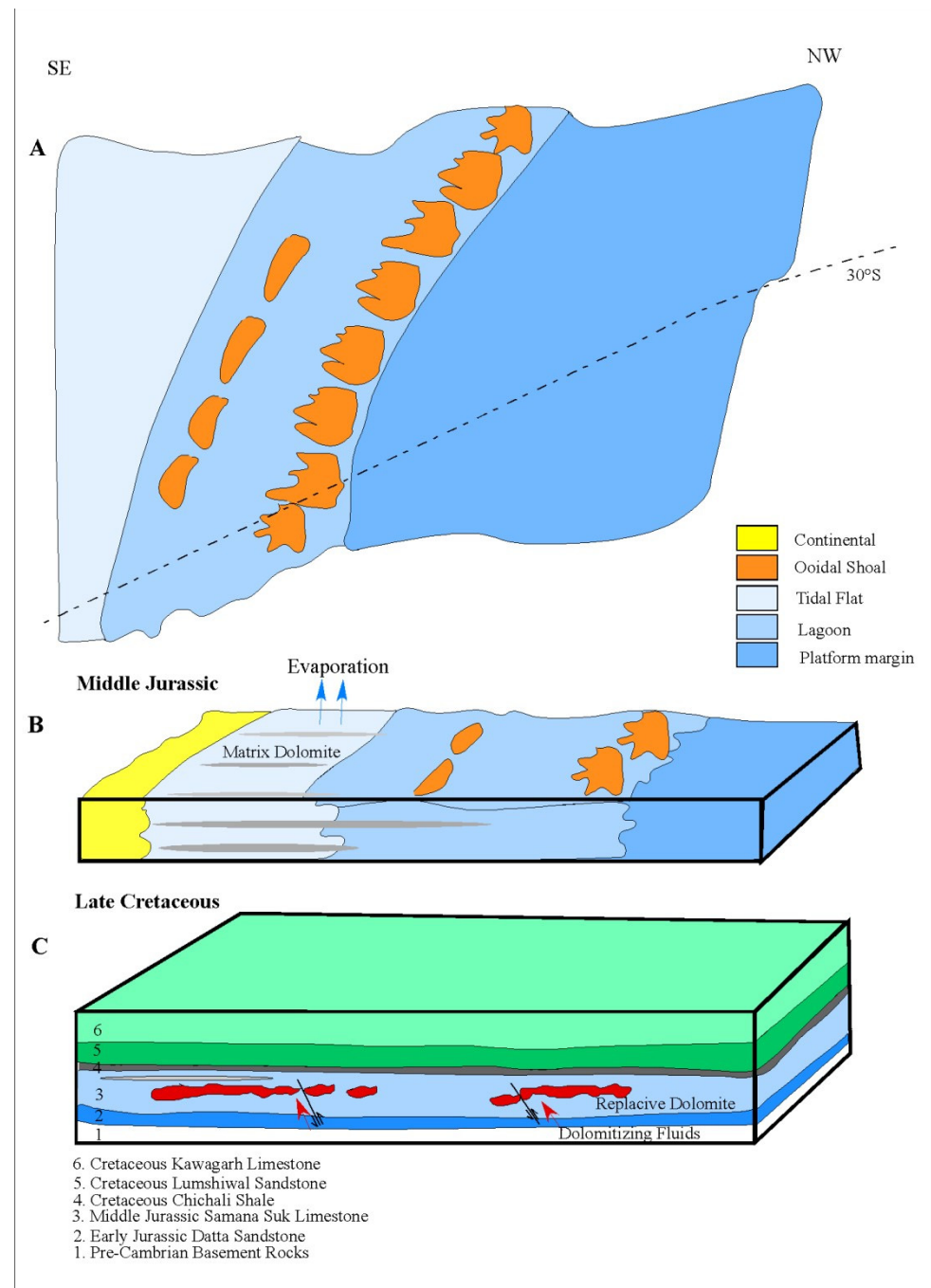
Figure 13. Model of multiphase dolomitization in the Samana Suk Formation (**A**). Paleogeographic reconstruction of the middle Jurassic of the northern margin of the Indian plate after Hussain, Fayaz, Haneef, Hanif, Jan, and Gul [31]. (**B**) A block diagram showing the formation of matrix dolomites. (**C**) The block diagram shows the formation of replacive and saddle dolomite channeled through fractures and faults.

In the case of hydrothermal dolomitization, the stratigraphic position plays an important role in the distribution of these hot fluids. Stratigraphically, the middle Jurassic Samana Suk Formation has lower transitional contact with the sandstones of the Datta Formation and upper disconformable contact with the Cretaceous shales of the Chichali Formation [71] (Figure 2). In the field observations, pervasive dolomitization is only observed in the Samana Suk Formation, while the Cretaceous and Tertiary successions are significantly undolomitized. The stratigraphic succession suggests that a possible source of dolomitizing fluids coming from the base, which was bounded on top by the thick shale units, which may have acted as aquitards for the further upward migration of the dolomitizing fluids, as suggested by Davies and Smith Jr [6]. The fluid source is cross-cutting the stratification and following the weak planes suggests that the dolomites are fracture-related (Figure 3C,D,F,G). This dolomitization process is reported in various classical studies of dolomitization [6,11,83,84].

As discussed above, replacive dolomite (RD-II) indicates its formation as a result of a hydrothermal process. Fe and Mn concentrations in the Samana Suk Formation limestone are very low, whereas, in the dolomites, they tend to increase in the matrix dolomite (RD-I) and are highest in the replacive dolomite RD (Figure 5B). This indicates the burial conditions associated with dolomitization in the reducing conditions. The δ^{13}C and δ^{18}O data of replacive dolomites fall between the low temperature and high temperature, as reported by Gregg et al. [85]. The significantly higher Sr isotope ratio of replacive dolomite and saddle dolomite suggests their fluid source is from more radiogenic lithology (Figure 8).

Fluid inclusion analysis can provide useful information about the source of dolomitizing fluids. However, due to their dark color and smaller-sized crystals, no homogenization temperature and last ice melting were measured in the matrix and replacive dolomite (RD-I and RD). However, their association with saddle dolomite (SD) containing measurable fluid inclusion of high homogenization temperature supports their formation in a similar environment (Figure 10A).

5.3. Dolomitizing Model

Results indicate that the dolomitization of the shallow marine carbonate succession resulted from a multistage process. Several models have been proposed to explain the dolomitization of platform carbonates [2,3,86]. The distinction among these models is the focus of scientific research in the field of carbonate sedimentology.

For matrix dolomite, the study area was located around the 30° S latitude and characterized by a semi-arid climate with periodic fluctuation [18] (Figure 13). The presence of cauliflower-shaped calcite and fenestral pores indicates the evaporitic setting. Such conditions favor the production of Mesohaline seawater with high salinity, which favors dolomitization by seawater reflux (Figure 13B).

Replacive and saddle dolomite are probably formed from hydrothermal fluids, likely derived from the Precambrian basement rocks and basal sandstones (Figure 13C). Those fluids were possibly channeled through fractures and faults that originated due to the tectonic activity in the Late Cretaceous [34]. Further movement of the hydrothermal fluids is retarded due to the active aquitards present in the stratification (Figures 2 and 13C).

6. Conclusions

The Jurassic Samana Suk Formation is extensively altered by the dolomitization process. Based on field, petrographic, and geochemical studies, the following conclusions can be drawn.

1. Dolomitization in the Jurassic Samana Suk Formation is a multiphase process, as revealed by field observations, petrographic studies, and geochemical analysis.
2. The first phase of dolomitization is initiated soon after the deposition and initial compaction of sediments because of altered seawater, which is supported by their presence as strata-bound units, small crystal size, higher Na concentration, low Fe

and Mn concentration, non-depleted δ^{18}O signatures, and non-radiogenic ^{87}Sr/^{86}Sr ratios.

3. The second phase of dolomitization resulted from hydrothermal sources as evidenced by the cross-cutting relationship in the field, large planer to non-planer crystal shape, lower concentration of Na and higher concentration of Mn and Fe, depleted δ^{18}O values, and radiogenic ^{87}Sr/^{86}Sr ratios.

4. The fluid inclusion analysis of saddle dolomite cement gives high temperature and salinity values, which suggest their formation from hydrothermal brines of high salinity.

5. The possible heat source can be linked to the hotspot igneous activity, which caused the domal uplift of the Indian plate during the Late Cretaceous. This causes activation of deep-seated faults, which causes the basement rich in brine fluids to move upward in the carbonate succession preferentially along fractures and dolomitize the succession.

6. Evaporite (gypsum, anhydrite) beds present in the Pre-Cambrian basement rocks can be the possible source for providing Mg-rich fluids during the burial of the carbonates.

7. Fractures and faults related to the Himalayan orogeny are steeply cross-cutting the limestone/dolostone succession. They are later filled with blocky calcite cement during uplift phases. The depleted δ^{18}O values, radiogenic ^{87}Sr/^{86}Sr ratios, and high homogenization temperature suggest their origin from hydrothermal sources.

References

1. Ahmad, I.; Shah, M.M.; Janjuhah, H.T.; Trave, A.; Antonarakou, A.; Kontakiotis, G. Multiphase Diagenetic Processes and Their Impact on Reservoir Character of the Late Triassic (Rhaetian) Kingriali Formation, Upper Indus Basin, Pakistan. *Minerals* **2022**, *12*, 1049. [CrossRef]
2. Warren, J. Dolomite: Occurrence, evolution and economically important associations. *Earth-Sci. Rev.* **2000**, *52*, 1–81. [CrossRef]
3. Machel, H.G. Concepts and models of dolomitization: A critical reappraisal. *Geol. Soc. Lond. Spec. Publ.* **2004**, *235*, 7–63. [CrossRef]
4. Rahim, H.u.; Shah, M.M.; Corbella, M.; Navarro-Ciurana, D. Diagenetic evolution and associated dolomitization events in the middle Jurassic Samana Suk Formation, Lesser Himalayan Hill Ranges, NW Pakistan. *Carbonates Evaporites* **2020**, *35*, 101. [CrossRef]
5. Cantrell, D.; Swart, P.; Hagerty, R. Genesis and characterization of dolomite, Arab-D reservoir, Ghawar field, Saudi Arabia. *GeoArabia* **2004**, *9*, 11–36. [CrossRef]
6. Davies, G.R.; Smith, L.B., Jr. Structurally controlled hydrothermal dolomite reservoir facies: An overview. *AAPG Bull.* **2006**, *90*, 1641–1690. [CrossRef]
7. Mahboubi, A.; Nowrouzi, Z.; Al-Aasm, I.; Moussavi-Harami, R.; Mahmudy-Gharaei, M. Dolomitization of the Silurian Niur Formation, Tabas block, east central Iran: Fluid flow and dolomite evolution. *Mar. Pet. Geol.* **2016**, *77*, 791–805. [CrossRef]
8. Shelton, K.L.; Cavender, B.D.; Perry, L.E.; Schiffbauer, J.D.; Appold, M.S.; Burstein, I.; Fike, D.A. Stable isotope and fluid inclusion studies of early Zn-Cu-(Ni-Co)-rich ores, lower ore zone of Brushy Creek mine, Viburnum Trend MVT district, Missouri, USA: Products of multiple sulfur sources and metal-specific fluids. *Ore Geol. Rev.* **2020**, *118*, 103358. [CrossRef]

9. Gasparrini, M.; Bakker, R.J.; Bechstädt, T. Characterization of dolomitizing fluids in the Carboniferous of the Cantabrian Zone (NW Spain): A fluid-inclusion study with cryo-Raman spectroscopy. *J. Sediment. Res.* **2006**, *76*, 1304–1322. [CrossRef]

10. Vandeginste, V.; Snell, O.; Hall, M.; Steer, E.; Vandeginste, A. Acceleration of dolomitization by zinc in saline waters. *Nat. Commun.* **2019**, *10*, 1851. [CrossRef]

11. Hendry, J.; Burgess, P.; Hunt, D.; Janson, X.; Zampetti, V. Seismic characterization of carbonate platforms and reservoirs: An introduction and review. *Geol. Soc. Lond. Spec. Publ.* **2021**, *509*, 1–28. [CrossRef]

12. Iannace, A.; Capuano, M.; Galluccio, L. "Dolomites and dolomites" in Mesozoic platform carbonates of the Southern Apennines: Geometric distribution, petrography and geochemistry. *Palaeogeogr. Palaeoclimatol. Palaeoecol.* **2011**, *310*, 324–339. [CrossRef]

13. Ryan, B.H.; Kaczmarek, S.E.; Rivers, J.M.; Manche, C.J. Extensive recrystallization of Cenozoic dolomite during shallow burial: A case study from the Palaeocene–Eocene Umm er Radhuma formation and a global meta-analysis. *Sedimentology* **2022**, *69*, 2053–2079. [CrossRef]

14. Purser, B.; Tucker, M.; Zenger, D. Problems, progress and future research concerning dolomites and dolomitization. *Dolomites A Vol. Honour Dolomieu* **1994**, *21*, 3–20.

15. Shah, M.M.; Ahmed, W.; Ahsan, N.; Lisa, M. Fault-controlled, bedding-parallel dolomite in the middle Jurassic Samana Suk Formation in Margalla Hill Ranges, Khanpur area (North Pakistan): Petrography, geochemistry, and petrophysical characteristics. *Arab. J. Geosci.* **2016**, *9*, 405. [CrossRef]

16. Ali, S.K.; Janjuhah, H.T.; Shahzad, S.M.; Kontakiotis, G.; Saleem, M.H.; Khan, U.; Zarkogiannis, S.D.; Makri, P.; Antonarakou, A. Depositional Sedimentary Facies, Stratigraphic Control, Paleoecological Constraints, and Paleogeographic Reconstruction of Late Permian Chhidru Formation (Western Salt Range, Pakistan). *J. Mar. Sci. Eng.* **2021**, *9*, 1372. [CrossRef]

17. Bilal, A.; Mughal, M.S.; Janjuhah, H.T.; Ali, J.; Niaz, A.; Kontakiotis, G.; Antonarakou, A.; Usman, M.; Hussain, S.A.; Yang, R. Petrography and Provenance of the Sub-Himalayan Kuldana Formation: Implications for Tectonic Setting and Palaeoclimatic Conditions. *Minerals* **2022**, *12*, 794. [CrossRef]

18. Saboor, A.; Ali, F.; Ahmad, S.; Haneef, M.; Hanif, M.; Imraz, M.; Ali, N.; Farooq Swati, M.A.; Zahid, M.; Sadiq, I. A preliminary account of the Middle Jurassic plays in Najafpur Village, southeastern Hazara, Khyber Pakhtunkhwa, Pakistan. *J. Himal. Earth Sci.* **2015**, *48*, 41–49.

19. Craig, J.; Hakhoo, N.; Bhat, G.; Hafiz, M.; Khan, M.; Misra, R.; Pandita, S.; Raina, B.; Thurow, J.; Thusu, B. Petroleum systems and hydrocarbon potential of the North-West Himalaya of India and Pakistan. *Earth-Sci. Rev.* **2018**, *187*, 109–185. [CrossRef]

20. Zaheer, M.; Khan, M.R.; Mughal, M.S.; Janjuhah, H.T.; Makri, P.; Kontakiotis, G. Petrography and Lithofacies of the Siwalik Group in the Core of Hazara-Kashmir Syntaxis: Implications for Middle Stage Himalayan Orogeny and Paleoclimatic Conditions. *Minerals* **2022**, *12*, 1055. [CrossRef]

21. Saleem, M.; Naseem, A.A.; Ahmad, W.; Yaseen, M.; Khan, T.U. Microfacies analysis, diagenetic overprints, geochemistry, and reservoir quality of the Jurassic Samanasuk Formation at the Kahi Section, Nizampur Basin, NW Himalayas, Pakistan. *Carbonates Evaporites* **2020**, *35*, 95.

22. Mateen, A.; Wahid, A.; Janjuhah, H.T.; Mughal, M.S.; Ali, S.H.; Siddiqui, N.A.; Shafique, M.A.; Koumoutsakou, O.; Kontakiotis, G. Petrographic and Geochemical Analysis of Indus Sediments: Implications for Placer Gold Deposits, Peshawar Basin, NW Himalaya, Pakistan. *Minerals* **2022**, *12*, 1059. [CrossRef]

23. Qureshi, M.K.A.; Butt, A.A.; Ghazi, S. Shallow shelf sedimentation of the Jurassic Samana Suk Limestone, Kala Chitta Range, Lesser Himalayas, Pakistan. *Geol. Bull. Punjab Univ.* **2008**, *43*, 1–14.

24. Yeats, R.S.; Hussain, A. Timing of structural events in the Himalayan foothills of northwestern Pakistan. *Geol. Soc. Am. Bull.* **1987**, *99*, 161–176. [CrossRef]

25. DiPietro, J.A.; Pogue, K.R. Tectonostratigraphic subdivisions of the Himalaya: A view from the west. *Tectonics* **2004**, *23*. [CrossRef]

26. Ghauri, A.; Pervez, M.; Riaz, M.; Rehman, O.; Ahmad, I.; Ahmad, S. The structure and tectonic setting of Attock-Cherat and Kalachitta ranges in Nizampur area, NWFP Pakistan. *Kashmir J. Geol.* **1991**, *8*, 99–109.

27. Searle, M.; Khan, M.A.; Fraser, J.; Gough, S.; Jan, M.Q. The tectonic evolution of the Kohistan-Karakoram collision belt along the Karakoram Highway transect, north Pakistan. *Tectonics* **1999**, *18*, 929–949. [CrossRef]

28. Ahsan, N.; Chaudhry, M.N. Geology of Hettangian to middle Eocene rocks of Hazara and Kashmir basins, Northwest lesser Himalayas, Pakistan. *Geol. Bull. Panjab Univ.* **2008**, *43*, 131–152.

29. Umar, M.; Sabir, M.A.; Farooq, M.; Khan, M.M.S.S.; Faridullah, F.; Jadoon, U.K.; Khan, A.S. Stratigraphic and sedimentological attributes in Hazara Basin Lesser Himalaya, North Pakistan: Their role in deciphering minerals potential. *Arab. J. Geosci.* **2015**, *8*, 1653–1667. [CrossRef]

30. Ahmed, F.; Ahmad, M.; Rahman, M.U.; Sarim, M.; Rehman, M.U.; Javed, M. Reservoir characterisation of lower cretaceous clastic succession of Nizampur Basin, Eastern Tethys; Pakistan. *J. Himal. Earth Sci.* **2017**, *50*, 44–59.

31. Hussain, H.S.; Fayaz, M.; Haneef, M.; Hanif, M.; Jan, I.U.; Gul, B. Microfacies and diagenetic-fabric of the Samana Suk Formation at Harnoi Section, Abbottabad, Khyber Pakhtunkhwa, Pakistan. *J. Himal. Earth Sci.* **2013**, *46*, 79.

32. Wadood, B.; Khan, S.; Li, H.; Liu, Y.; Ahmad, S.; Jiao, X. Sequence stratigraphic framework of the Jurassic Samana Suk carbonate formation, North Pakistan: Implications for reservoir potential. *Arab. J. Sci. Eng.* **2021**, *46*, 525–542. [CrossRef]

33. Ali, J.R.; Aitchison, J.C. Gondwana to Asia: Plate tectonics, paleogeography and the biological connectivity of the Indian sub-continent from the Middle Jurassic through latest Eocene (166–35 Ma). *Earth-Sci. Rev.* **2008**, *88*, 145–166. [CrossRef]

34. Chatterjee, S.; Goswami, A.; Scotese, C.R. The longest voyage: Tectonic, magmatic, and paleoclimatic evolution of the Indian plate during its northward flight from Gondwana to Asia. *Gondwana Res.* **2013**, *23*, 238–267. [CrossRef]

35. Garzanti, E. Sedimentary evolution and drowning of a passive margin shelf (Giumal Group; Zanskar Tethys Himalaya, India): Palaeoenvironmental changes during final break-up of Gondwanaland. *Geol. Soc. Lond. Spec. Publ.* **1993**, *74*, 277–298. [CrossRef]

36. Ghose, N.C.; Chatterjee, N.; Windley, B.F. Subaqueous early eruptive phase of the late Aptian Rajmahal volcanism, India: Evidence from volcaniclastic rocks, bentonite, black shales, and oolite. *Geosci. Front.* **2017**, *8*, 809–822. [CrossRef]

37. Jan, M.Q.; Windley, B.F.; Khan, A. The Waziristan ophiolite, Pakistan; general geology and chemistry of chromite and associated phases. *Econ. Geol.* **1985**, *80*, 294–306. [CrossRef]

38. Janjuhah, H.T. Sedimentology and Origin of Microporosity in Miocene Carbonate Platforms, Central Luconia, Offshore Sarawak, Malaysia. Ph.D. Thesis, Universiti Teknologi PETRONAS, Seri Iskandar, Malaysia, 2018.

39. Saboor, A.; Haneef, M.; Hanif, M.; Swati, M.A.F. Sedimentological attributes of the Middle Jurassic peloids-dominated carbonates of eastern Tethys, lesser Himalayas, Pakistan. *Carbonates Evaporites* **2020**, *35*, 123. [CrossRef]

40. Janjuhah, H.T.; Alansari, A. Offshore carbonate facies characterization and reservoir quality of Miocene rocks in the southern margin of South China Sea. *Acta Geol. Sin.-Engl. Ed.* **2020**, *94*, 1547–1561. [CrossRef]

41. Janjuhah, H.T.; Sanjuan, J.; Alqudah, M.; Salah, M.K. Biostratigraphy, Depositional and Diagenetic Processes in Carbonate Rocks from Southern Lebanon: Impact on Porosity and Permeability. *Acta Geol. Sin.-Engl. Ed.* **2021**, *95*, 1668–1683. [CrossRef]

42. Sibley, D.F.; Gregg, J.M. Classification of dolomite rock textures. *J. Sediment. Res.* **1987**, *57*, 967–975.

43. Flügel-Martinsen, O. Demokratie und Dissens Zur Kritik konsenstheoretischer Prämissen der deliberativen Demokratietheorie. In *Proceedings of the Die Versprechen der Demokratie*; Nomos: Baden-Baden, Germany, 2013; pp. 332–345.

44. Rosenbaum, J.; Sheppard, S. An isotopic study of siderites, dolomites and ankerites at high temperatures. *Geochim. Et Cosmochim. Acta* **1986**, *50*, 1147–1150. [CrossRef]

45. Roedder, E. Volume 12: Fluid inclusions. *Rev. Mineral.* **1984**, *12*, 644.

46. Bodnar, R.J.; Samson, I.; Anderson, A.; Marshall, D. Introduction to aqueous-electrolyte fluid inclusions. *Fluid Incl. Anal. Interpret.* **2003**, *32*, 81–100.

47. Védrine, S.; Strasser, A.; Hug, W. Oncoid growth and distribution controlled by sea-level fluctuations and climate (Late Oxfordian, Swiss Jura Mountains). *Facies* **2007**, *53*, 535–552. [CrossRef]

48. Madden, R.H.; Wilson, M.E. Diagenesis of a SE Asian Cenozoic carbonate platform margin and its adjacent basinal deposits. *Sediment. Geol.* **2013**, *286*, 20–38. [CrossRef]

49. Janjuhah, H.T.; Kontakiotis, G.; Wahid, A.; Khan, D.M.; Zarkogiannis, S.D.; Antonarakou, A. Integrated Porosity Classification and Quantification Scheme for Enhanced Carbonate Reservoir Quality: Implications from the Miocene Malaysian Carbonates. *J. Mar. Sci. Eng.* **2021**, *9*, 1410. [CrossRef]

50. Al-Mojel, A.; Dera, G.; Razin, P.; Le Nindre, Y.-M. Carbon and oxygen isotope stratigraphy of Jurassic platform carbonates from Saudi Arabia: Implications for diagenesis, correlations and global paleoenvironmental changes. *Palaeogeogr. Palaeoclimatol. Palaeoecol.* **2018**, *511*, 388–402. [CrossRef]

51. McArthur, J.; Howarth, R.; Shields, G. Strontium isotope stratigraphy. *Geol. Time Scale* **2012**, *1*, 127–144.

52. Gregg, J.M.; Shelton, K.L. Dolomitization and dolomite neomorphism in the back reef facies of the Bonneterre and Davis formations (Cambrian), southeastern Missouri. *J. Sediment. Res.* **1990**, *60*, 549–562.

53. Zheng, H.; Ma, Y.; Chi, G.; Qing, H.; Liu, B.; Zhang, X.; Shen, Y.; Liu, J.; Wang, Y. Stratigraphic and structural control on hydrothermal Dolomitization in the middle Permian carbonates, southwestern Sichuan Basin (China). *Minerals* **2019**, *9*, 32. [CrossRef]

54. Van Lith, Y.; Vasconcelos, C.; Warthmann, R.; Martins, J.; McKenzie, J. Bacterial sulfate reduction and salinity: Two controls on dolomite precipitation in Lagoa Vermelha and Brejo do Espinho (Brazil). *Hydrobiologia* **2002**, *485*, 35–49. [CrossRef]

55. Liang, F.; Niu, J.; Linsel, A.; Hinderer, M.; Scheuvens, D.; Petschick, R. Rock alteration at the post-Variscan nonconformity: Implications for Carboniferous—Permian surface weathering versus burial diagenesis and paleoclimate evaluation. *Solid Earth* **2021**, *12*, 1165–1184. [CrossRef]

56. Tucker, M.E. Diagenesis, geochemistry, and origin of a Precambrian dolomite; the Beck Spring Dolomite of eastern California. *J. Sediment. Res.* **1983**, *53*, 1097–1119.

57. Brand, U.; Veizer, J. Chemical diagenesis of a multicomponent carbonate system; 1, Trace elements. *J. Sediment. Res.* **1980**, *50*, 1219–1236.

58. Land, L.S. Contemporaneous dolomitization of middle Pleistocene reefs by meteoric water, north Jamaica. *Bull. Mar. Geol.* **1973**, *23*, 64–92.

59. Smrzka, D.; Zwicker, J.; Bach, W.; Feng, D.; Himmler, T.; Chen, D.; Peckmann, J. The behavior of trace elements in seawater, sedimentary pore water, and their incorporation into carbonate minerals: A review. *Facies* **2019**, *65*, 41. [CrossRef]

60. Frisia, S.; Borsato, A.; Drysdale, R.; Paul, B.; Greig, A.; Cotte, M. A re-evaluation of the palaeoclimatic significance of phosphorus variability in speleothems revealed by high-resolution synchrotron micro XRF mapping. *Clim. Past* **2012**, *8*, 2039–2051. [CrossRef]

61. Veizer, J.; Ala, D.; Azmy, K.; Bruckschen, P.; Buhl, D.; Bruhn, F.; Carden, G.A.F.; Diener, A.; Ebneth, S.; Godderis, Y.; et al. Sr^{86}/Sr^{87}, $\delta^{13}C$ and $\delta^{18}O$ evolution of Phanerozoic seawater. *Chemi. Geol.* **1999**, *87*, 59–88. [CrossRef]

62. Gasparrini, M.; Bechstädt, T.; Boni, M. Massive hydrothermal dolomites in the southwestern Cantabrian Zone (Spain) and their relation to the Late Variscan evolution. *Mar. Pet. Geol.* **2006**, *23*, 543–568. [CrossRef]

63. Chen, D.; Qing, H.; Yang, C. Multistage hydrothermal dolomites in the Middle Devonian (Givetian) carbonates from the Guilin area, South China. *Sedimentology* **2004**, *51*, 1029–1051. [CrossRef]

64. Barnaby, R.J.; Oetting, G.C.; Gao, G. Strontium isotopic signatures of oil-field waters: Applications for reservoir characterization. *AAPG Bull.* **2004**, *88*, 1677–1704. [CrossRef]

65. Gregg, J.M.; Bish, D.L.; Kaczmarek, S.E.; Machel, H.G. Mineralogy, nucleation and growth of dolomite in the laboratory and sedimentary environment: A review. *Sedimentology* **2015**, *62*, 1749–1769. [CrossRef]

66. Mountjoy, E.; Amthor, J.; Machel, H. Has burial dolomitization come of age? Some answers from the Western Canada sedimentary basin. In *Dolomites: A Volume in Honour of Dolomieu*; Purser, B., Tucker, M., Zenger, D., Eds.; Wiley Online Library: Hoboken, NJ, USA, 1994; pp. 203–229.

67. Iqbal, S.; Jan, I.U.; Akhter, M.G.; Bibi, M. Palaeoenvironmental and sequence stratigraphic analyses of the Jurassic Datta formation, Salt Range, Pakistan. *J. Earth Syst. Sci.* **2015**, *124*, 747–766. [CrossRef]

68. Janjuhah, H.T.; Alansari, A.; Santha, P.R. Interrelationship between facies association, diagenetic alteration and reservoir properties evolution in the Middle Miocene carbonate build up, Central Luconia, Offshore Sarawak, Malaysia. *Arab. J. Sci. Eng.* **2019**, *44*, 341–356. [CrossRef]

69. Liu, S.; Huang, S.; Shen, Z.; Lü, Z.; Song, R. Diagenetic fluid evolution and water-rock interaction model of carbonate cements in sandstone: An example from the reservoir sandstone of the Fourth Member of the Xujiahe Formation of the Xiaoquan-Fenggu area, Sichuan Province, China. *Sci. China Earth Sci.* **2014**, *57*, 1077–1092. [CrossRef]

70. Pache, M.; Reitner, J.; Arp, G. Geochemical evidence for the formation of a large Miocene "travertine" mound at a sublacustrine spring in a soda lake (Wallerstein Castle Rock, Nördlinger Ries, Germany). *Facies* **2001**, *45*, 211–230. [CrossRef]

71. Shah, M.M.; Afridi, S.; Khan, E.U.; Rahim, H.U.; Mustafa, M.R. Diagenetic modifications and reservoir heterogeneity associated with magmatic intrusions in the Devonian Khyber Limestone, Peshawar Basin, NW Pakistan. *Geofluids* **2021**, *2021*, 8816465. [CrossRef]

72. Ryb, U.; Eiler, J.M. Oxygen isotope composition of the Phanerozoic ocean and a possible solution to the dolomite problem. *Proc. Natl. Acad. Sci. USA* **2018**, *115*, 6602–6607. [CrossRef]

73. Ahmad, W.; Ullah, S.; Ahmad, I.; Gingras, M.K.; Shafique, M.; Khan, E.U.; Shah, M. Reflux dolomitization and subsequent hydrothermal dolomitization induced by the Alkaline Igneous Province in the Middle Devonian Nowshera Formation (Peshawar Basin, NW Pakistan). *Mar. Pet. Geol.* **2021**, *131*, 105178. [CrossRef]

74. Friedman, I.; O'Neil, J.R. *Compilation of Stable Isotope Fractionation Factors of Geochemical Interest*; US Government Printing Office: Washington, DC, USA, 1977; Volume 440.

75. Courtillot, V.E.; Renne, P.R. On the ages of flood basalt events. *Comptes Rendus Geosci.* **2003**, *335*, 113–140. [CrossRef]

76. Besse, J.; Courtillot, V. Revised and synthetic apparent polar wander paths of the African, Eurasian, North American and Indian plates, and true polar wander since 200 Ma. *J. Geophys. Res. Solid Earth* **1991**, *96*, 4029–4050. [CrossRef]

77. Srivastava, R.K.; Kumar, S.; Sinha, A.K.; Rao, N.C. Petrology and geochemistry of high-titanium and low-titanium mafic dykes from the Damodar valley, Chhotanagpur Gneissic Terrain, eastern India and their relation to Cretaceous mantle plume (s). *J. Asian Earth Sci.* **2014**, *84*, 34–50. [CrossRef]

78. Nader, F.H.; Swennen, R.; Ellam, R.M.; Immenhauser, A. Field geometry, petrography and geochemistry of a dolomitization front (Late Jurassic, central Lebanon). *Sedimentology* **2007**, *54*, 1093–1120. [CrossRef]

79. Machel, H.-G.; Mountjoy, E.W. Chemistry and environments of dolomitization—A reappraisal. *Earth-Sci. Rev.* **1986**, *23*, 175–222. [CrossRef]

80. Kaczmarek, S.E.; Gregg, J.M.; Bish, D.L.; Machel, H.G.; Fouke, B.W.; MacNeil, A.; Lonnee, J.; Wood, R. Dolomite, very-high magnesium calcite, and microbes: Implications for the microbial model of dolomitization. In Proceedings of the Characterization and Modeling of Carbonates–Mountjoy Symposium, Austin, TX, USA, 25–29 June 2017; pp. 7–20.

81. Han, Z.; Hu, X.; Li, J.; Garzanti, E. Jurassic carbonate microfacies and relative sea-level changes in the Tethys Himalaya (southern Tibet). *Palaeogeogr. Palaeoclimatol. Palaeoecol.* **2016**, *456*, 1–20. [CrossRef]

82. Janjuhah, H.T.; Gamez Vintaned, J.A.; Salim, A.M.A.; Faye, I.; Shah, M.M.; Ghosh, D.P. Microfacies and depositional environments of miocene isolated carbonate platforms from Central Luconia, Offshore Sarawak, Malaysia. *Acta Geol. Sin.-Engl. Ed.* **2017**, *91*, 1778–1796. [CrossRef]

83. López-Horgue, M.; Iriarte, E.; Schröder, S.; Fernández-Mendiola, P.; Caline, B.; Corneyllie, H.; Frémont, J.; Sudrie, M.; Zerti, S. Structurally controlled hydrothermal dolomites in Albian carbonates of the Asón valley, Basque Cantabrian Basin, Northern Spain. *Mar. Pet. Geol.* **2010**, *27*, 1069–1092. [CrossRef]

84. Martín-Martín, J.D.; Travé, A.; Gomez-Rivas, E.; Salas, R.; Sizun, J.-P.; Vergés, J.; Corbella, M.; Stafford, S.; Alfonso, P. Fault-controlled and stratabound dolostones in the Late Aptian–earliest Albian Benassal Formation (Maestrat Basin, E Spain): Petrology and geochemistry constrains. *Mar. Pet. Geol.* **2015**, *65*, 83–102. [CrossRef]

85. Gregg, J.M.; Shelton, K.L.; Johnson, A.W.; Somerville, I.D.; Wright, W.R. Dolomitization of the Waulsortian limestone (lower Carboniferous) in the Irish Midlands. *Sedimentology* **2001**, *48*, 745–766. [CrossRef]

86. Budd, D. Cenozoic dolomites of carbonate islands: Their attributes and origin. *Earth-Sci. Rev.* **1997**, *42*, 1–47. [CrossRef]